Resolving high-frequency internal waves generated at an isolated coral atoll using an unstructured grid ocean model

Matthew D. Rayson[*,a], Gregory N. Ivey[a], Nicole L. Jones[a], Oliver B. Fringer[b]

[a] School of Civil, Environmental and Mining Engineering and The Oceans Institute, University of Western Australia, Crawley, WA, Australia
[b] Bob and Norma Street Environmental Fluid Mechanics Laboratory, Department of Civil and Environmental Engineering, Stanford University, Stanford, CA, United States

ARTICLE INFO

ABSTRACT

We apply the unstructured grid hydrodynamic model SUNTANS to investigate the internal wave dynamics around Scott Reef, Western Australia, an isolated coral reef atoll located on the edge of the continental shelf in water depths of 500,m and more. The atoll is subject to strong semi-diurnal tidal forcing and consists of two relatively shallow lagoons separated by a 500 m deep, 2 km wide and 15 km long channel. We focus on the dynamics in this channel as the internal tide-driven flow and resulting mixing is thought to be a key mechanism controlling heat and nutrient fluxes into the reef lagoons. We use an unstructured grid to discretise the domain and capture both the complex topography and the range of internal wave length scales in the channel flow. The model internal wave field shows super-tidal frequency lee waves generated by the combination of the steep channel topography and strong tidal flow. We evaluate the model performance using observations of velocity and temperature from two through water-column moorings in the channel. Three different global ocean state estimate datasets (global HYCOM, CSIRO Bluelink, CSIRO climatology atlas) were used to provide the model initial and boundary conditions, and the model outputs from each were evaluated against the field observations. The scenario incorporating the CSIRO Bluelink data performed best in terms of through-water column Murphy skill scores of water temperature and eastward velocity variability in the channel. The model captures the observed vertical structure of the tidal (M_2) and super-tidal (M_4) frequency temperature and velocity oscillations. The model also predicts the direction and magnitude of the M_2 internal tide energy flux. An energy analysis reveals a net convergence of the M_2 energy flux and a divergence of the M_4 energy flux in the channel, indicating the channel is a region of either energy transfer to higher frequencies or energy loss to dissipation. This conclusion is supported by the mooring observations that reveal high frequency lee waves breaking on the turning phase of the tide.

1. Introduction

Topographic internal wave generation occurs at length-scales ranging from $\sim O(0.1$–$100)$ km. Important parameters that influence the type of internal wave response include the tidal excursion ratio, the ratio of the internal wave characteristic slope to topographic slope, and the topographic Froude number Legg and Klymak (see e.g., 2008); Winters and Armi (see e.g., 2013). In regions where these parameters are all of order one, nonlinear effects due to advection influence the generation process. Lee waves, characterized by higher frequency harmonics, form when internal wave generation is affected by barotropic advection (Bell, 1975). These transient lee waves formed by oscillatory flow are referred to as tidal lee waves in the literature (Nakamura and Awaji, 2001). Other phenomena, including transient hydraulic jumps and internal wave breaking, have been observed in locations such as the

Hawaiian Ridge (Alford et al., 2014), the Luzon Strait (Buijsman et al., 2012) and the Mendocino Escarpment (Musgrave et al., 2016). Coral atolls and island chains along continental slopes fall within this regime of the flow parameter space, a regime where vertical mixing is likely to be enhanced and, in turn, can have a strong influence on the local ecology (e.g., Gove et al., 2016).

Three-dimensional Reynolds-averaged Navier–Stokes (RANS) ocean models in island regions must therefore resolve the wide range of topographic length scales to adequately capture the internal wave generation process. The models also need to capture the larger scale background forcing processes, such as the shelf-scale barotropic and baroclinic (internal) tides plus the regional mesoscale circulation. RANS models that employ an unstructured grid discretization are particularly suitable for this task. Furthermore, island atolls are often steep-sided with topographic gradients as large as 50%, meaning that models using

---

sigma-coordinate vertical discretization have strict horizontal resolution requirements due to pressure gradient calculation issues (see e.g., Shchepetkin and McWilliams, 2003).

Modeling the time-varying flow of the tidally-driven, stratified flow around and through the channel at the steep-sided Scott Reef atoll system is the focus of this paper. The key differences between Scott Reef and other channel sites, such as at the mouth of an estuary or an ocean strait, are that the reef is located in the open ocean, the water column is continuously stratified and, as opposed to forcing from a horizontal density gradient, a large-amplitude barotropic tide drives an unsteady flow through this channel. At Scott Reef the tidal excursion distance is comparable to the length scale of the channel. To model these processes, one must capture the shelf-scale circulation, the tidal forcing, and the internal tides, while also resolving all the topographic length scales of interest.

The long-term motivation here is to understand the internal wave-driven vertical mixing near coral reef systems that are particularly sensitive to ocean warming caused by climate change (Hughes et al., 2017). Identifying topographically-induced mixing processes will help identify regions within a reef that are less susceptible to surface warming because cooler water can be lifted from depth to mix with warm surface waters. A first step is to model the transfer of the internal tide energy into higher frequencies and wavenumbers that are more conducive to dissipation and small-scale mixing. The next step, and beyond the scope here, is to quantify the mixing rates associated with the breaking of the internal waves (e.g., Sarkar and Scotti, 2017).

In Section 2 of this paper, we give an overview of the study region and present the numerical model setup procedure. In Section 3, we present a quantitative comparison between the numerical model and the through water-column mooring observations collected during a field experiment in April 2015. A description of the internal tide dynamics in the channel is then presented in Section 4, along with model estimates of the internal wave energy generated by the island topography. We conclude with a brief discussion of the dynamics and overview of the model performance.

2. Methods

2.1. Study site

Scott Reef is an island atoll reef system lying on the edge of the continental shelf in water depths of 500 m (see Fig. 1). It is one of several offshore reef systems along the shelf edge of the Australian North West Shelf - Timor Sea region. The reefs have continued to grow despite being situated on a subsiding shelf (Collins and Testa, 2010). The topography of Scott Reef consists of two near-circular reefs, North and South Scott Reef, with dimensions 38 km from north to south, and 28 km from east to west. South Scott Reef, the larger of the two reefs, has a deep lagoon with an average depth of 40 m, which is open along its northern side. The two reefs are separated by a 500 m deep channel approximately 15 km in length from east to west and 2 km wide at its narrowest point. Corals in the lagoons were affected during both the 1998 and 2016 global bleaching events (Gilmour et al., 2013; Hughes et al., 2017, respectively).
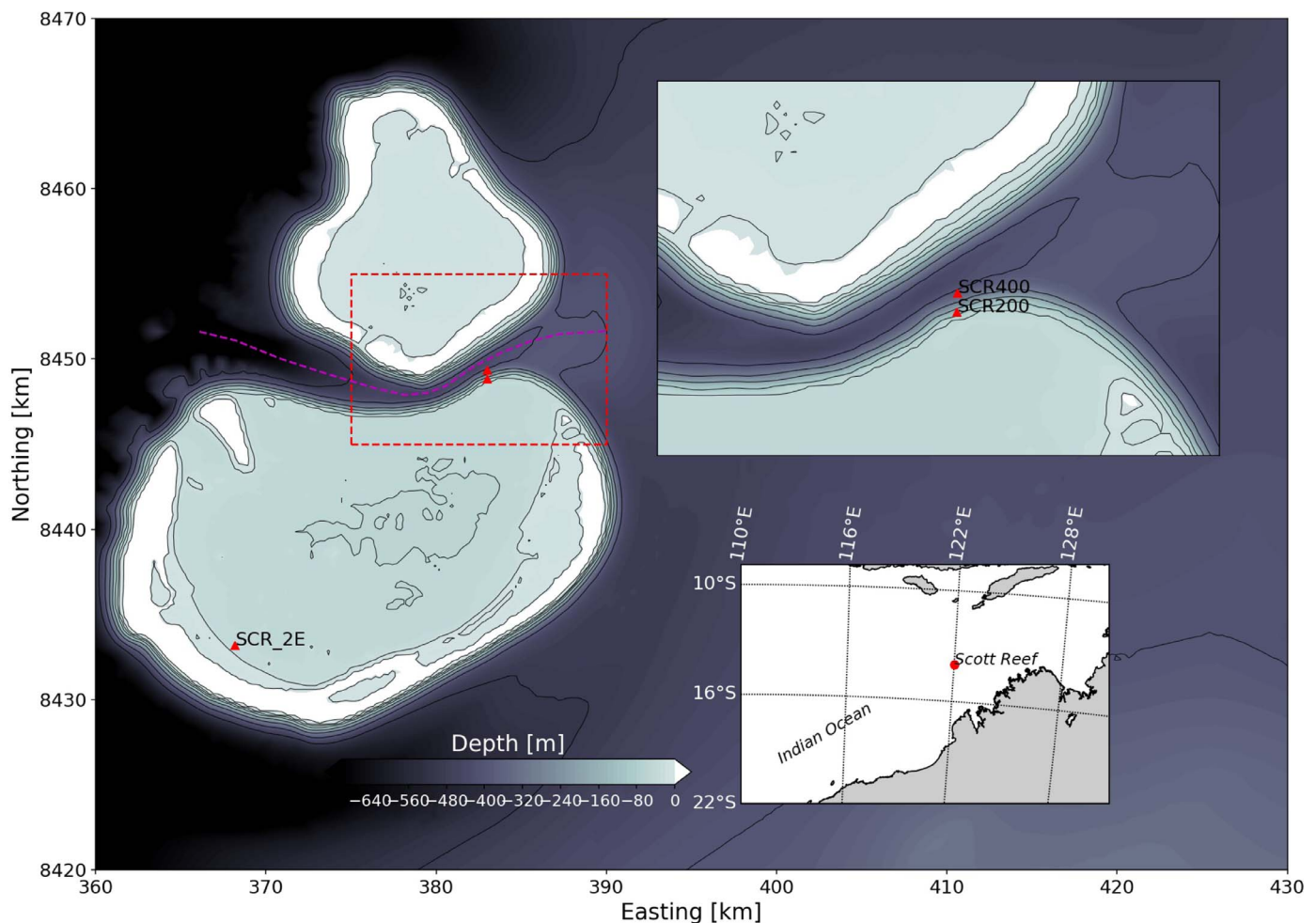

Fig. 1. Bathymetric contour map of Scott Reef with mooring locations indicated by red triangles. The red dashed box indicates the region in the top-right inset panel. The purple dashed line indicates the channel *thalweg*.

Rayson et al. (2011) used a 2 km resolution ROMS model with a smoothed representation of Scott Reef to study the regional dynamics around the reef. The oceanography of the region is dominated by a strong semi-diurnal (M_2 and S_2) tide with a tidal range at Scott Reef of 4 m. The semi-diurnal barotropic tidal currents on the shelf around the reef are in the range of 0.15–0.20 m s^{-1} at the 500 m isobath. In Rayson et al. (2011), field measurements and numerical modeling revealed the presence of an energetic internal tide on the surrounding continental shelf and on the outer flanks of the reef.

The important geometric parameters of the channel are the length L, depth $H(x)$, and the width at both the surface $b_0(x)$ and through the water column, $b(x, z)$. Representative values for H and L are 450 m and 15 km, respectively, and the bottom slopes down at the western entrance (Fig. 2a). The width at the surface $b_0(x)$ varies between 2 and 6 km, with the narrowest section located between easting 379 and 382 km. The channel width varies with depth and can be approximated by a parabolic profile in the main contraction and by a rectangular-like profile towards the entrances (Fig. 2b). The width of the channel is asymmetric with $b_0(x)$ diverging more rapidly at the eastern exit than at the western exit ($\partial b_0/\partial x \approx 1.0$ and 0.4, respectively). The channel bends at the point of maximum contraction with a radius of curvature $R \approx 5$ km. Curvature effects may also contribute to the mixing in the channel although they are not the primary focus here (see e.g., Edwards et al., 2004).

A preview of the isotherm displacement and along channel velocity from the SUNTANS model is shown in Fig. 2c. Lee waves are evident in the eastern divergent section of the channel at around easting 385 km. The internal Froude number $Fr_n = \bar{u}/c_n$, where $\bar{u}$ is the maximum barotropic velocity from the model and c_n is the internal wave phase speed of mode-n (Gill, 1982), is shown as a function of distance along the channel in Fig. 2d. The second baroclinic mode transitions from super-critical ($Fr_2 > 1$) to sub-critical ($Fr_2 < 1$) near the tidal lee wave generation region indicating that trapping of mode-two waves is likely and hydraulic effects are important. Much of the focus for the rest of the paper is on the tidal lee wave evolution process and model-data comparison in this particular region.

2.2. Field observations

Two moorings were deployed in the channel during a research cruise in April 2015 aboard the *RV Falkor*, operated by the Schmidt Ocean Institute. These measurements were taken in conjunction with other bio-physical measurements around Scott Reef as part of a broader study to understand the connections between the physical processes and the ecosystem dynamics of Australia's Northern reef systems. The two moorings were positioned near the 400 m and 200 m isobaths labelled SCR400 and SCR200, respectively in Fig. 1. The mooring locations were chosen based on the most energetic regions identified using an earlier version of the SUNTANS model described here (Rayson, 2012). We are now using the observations to evaluate the model performance and characterise the internal waves in the channel. This is the first paper to show this set of observations.

The SCR400 mooring consisted of 19 temperature instruments (Seabird Electronics SBE56, 39 and 37), six pressure instruments (SBE39P and 37), and two conductivity (SBE37) sensors. Velocity in the lower 200 m was measured with a downward-looking RDI 75 kHz Long Ranger ADCP, and velocity in the upper 170 m was measured with an upward-looking RDI 300 kHz WorkHorse ADCP. This ADCP configuration was chosen to maximize flotation in the upper section of the mooring as the Long Ranger was buoy-mounted. The SCR200 mooring was positioned 500 m south of SCR400 on the edge of the channel where the side wall slope gradient was roughly 25%. This mooring consisted of four pressure, 11 temperature, and two conductivity sensors, and velocity was measured with an upward-looking RDI 150 kHz QuarterMaster moored 4 m above the seabed. Pressure was recorded at several fixed-seabed locations around the lagoon using a RBR-Solo

instrument although we have used one (SCR2E) as a reference water level station.

At peak flows, the very strong currents in excess of 1.5 m s^{-1} knocked the SCR400 mooring down by up to 100 m; we evaluated the vertical displacement via pressure measurements at six locations from 20 m below the surface to 100 m above the seabed. Using these six pressure measurements, the temperature observations were then mapped onto a Lagrangian vertical coordinate. ADCP measurements were omitted from the analyses when the instrument tilt due to knockdown was greater than 20°. Knockdown was less severe at the SCR200 mooring, although peak currents during ebb tides (westward flow) led to some loss of velocity data.

2.3. Numerical model setup

We used the SUNTANS hydrodynamic model code described in Fringer et al. (2006) for the present study. SUNTANS solves the three-dimensional Reynolds-averaged Navier–Stokes equations on an unstructured horizontal domain and fixed z-level vertical domain using a finite-volume/finite-difference discretization. A semi-implicit time-stepping scheme is used to update the free-surface efficiently and high-order flux-limiting schemes are used for tracer advection. The model can solve the full vertical momentum equation and hence the non-hydrostatic pressure, although this was not necessary for the horizontal grid scale of the present application. SUNTANS has been used for various hydrodynamic studies of estuarine circulation (e.g., Rayson et al., 2015; Holleman et al., 2013; Wang et al., 2011), and internal waves (e.g., Zhang et al., 2011; Kang and Fringer, 2012). Other than these examples, there are few regional unstructured grid modeling studies for this type of realistic shelf-scale application in the literature.

2.3.1. Model grid

The SUNTANS unstructured mesh used in this study is shown in Fig. 3. The mesh was composed of n-sided, mainly hexagonal, cells. Here, we will refer to this mesh as the hexagonal or hex mesh although, strictly speaking, the grid was also composed of other n-sided polygons. Wolfram and Fringer (2013) showed that non-triangular meshes reduce numerical error in the horizontal divergence calculation in unstructured finite-volume models using an Arakawa-C grid. The reduction in horizontal divergence error, in turn, reduces vertical velocity errors. Rayson et al. (2015) used a mixed triangular-quadrilateral grid in an estuarine application and showed better skill than a comparable triangle-only grid. This is the first published study using an n-sided grid with the SUNTANS model, although the Los Alamos MPAS-Ocean model now routinely uses this type of grid (Ringler et al., 2013).

The triangular dual-grid was first constructed using the TOM triangular paving algorithm described in Holleman et al. (2013). The hexagonal mesh was then generated by taking the dual of the triangular mesh i.e, nodes of the triangular grid became cell-centres of the hex mesh and vice-versa (see Fig. 3d as an example). Inputs into the triangular grid generation code include a boundary polygon and a series of spatial lines that specify the target grid resolution in different parts of the domain. Using these inputs, TOM generates a near-perfect orthogonal unstructured mesh that smoothly transitions between regions of different resolution with a specified, maximum stretching rate; we used a rate of 3%. The geometric and topological properties of the resultant grid make it numerically efficient and stable for the finite-volume formulation used in SUNTANS.

The horizontal resolution (the distance between cell centres) transitioned from roughly 5000 m at the open boundary down to 100 m around Scott Reef itself (Fig. 3). The inter-tidal reef platforms on North and South Scott Reef were masked out and used as an internal land boundary to avoid the numerical issues associated with free-surface wetting and drying. The final hexagonal mesh consisted of 82,164 total horizontal cells with 165,753 nodes (the triangular dual mesh had this many cells). The vertical coordinate was discretised using 100 fixed z-
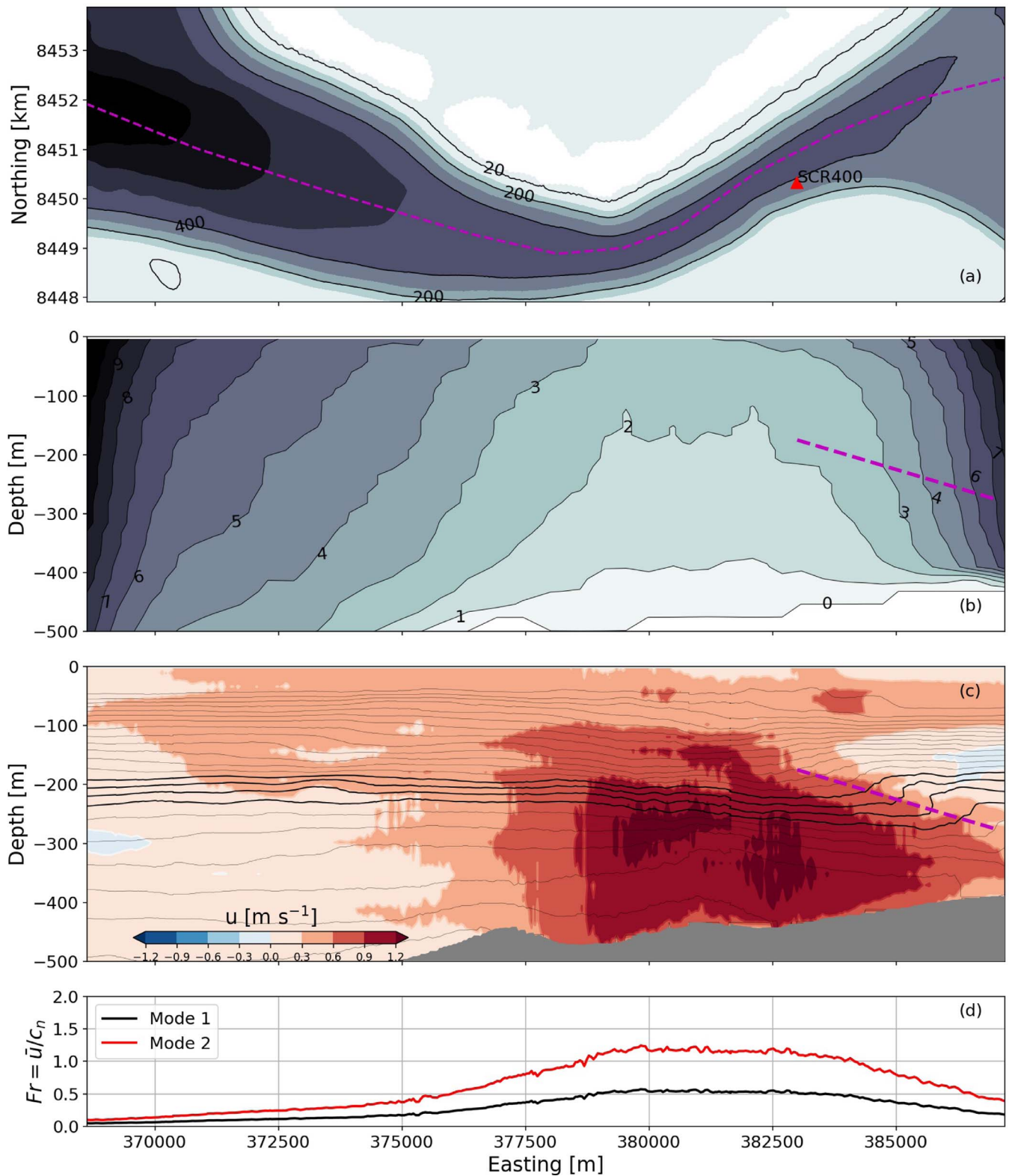
Fig. 2. (a) Zoom in on the channel bathymetry with (b) the width [km] as a function of distance and depth. (c) A snapshot of model eastward velocity with isotherms overlaid during a flood tide period. The pink dashed line in (b) and (c) indicates the approximate lee wave generation region on the eastern end of the channel. (d) Internal Froude number for the first two baroclinic modes as a function of distance along the channel. (For interpretation of the references to color in this figure legend, the reader is referred to the web version of this article).

layers with a resolution $\Delta z = 7$ m at the surface that increased by a stretching factor $r = 1.034$ down to the maximum depth (roughly 5500 m). The approximate vertical resolution at 400 m, where the deepest observations were located, was roughly 20 m. The 3D model domain consisted of 2,150,409 total grid cells.

2.3.2. Bathymetry

Bathymetry data for the region was sourced from a Geoscience Australia (GA) gridded 250 m dataset (2009) that covered the entire region, an incomplete Geoscience Australia gridded 50 m multibeam dataset, and a 10 m resolution blended multibeam and LIDAR dataset
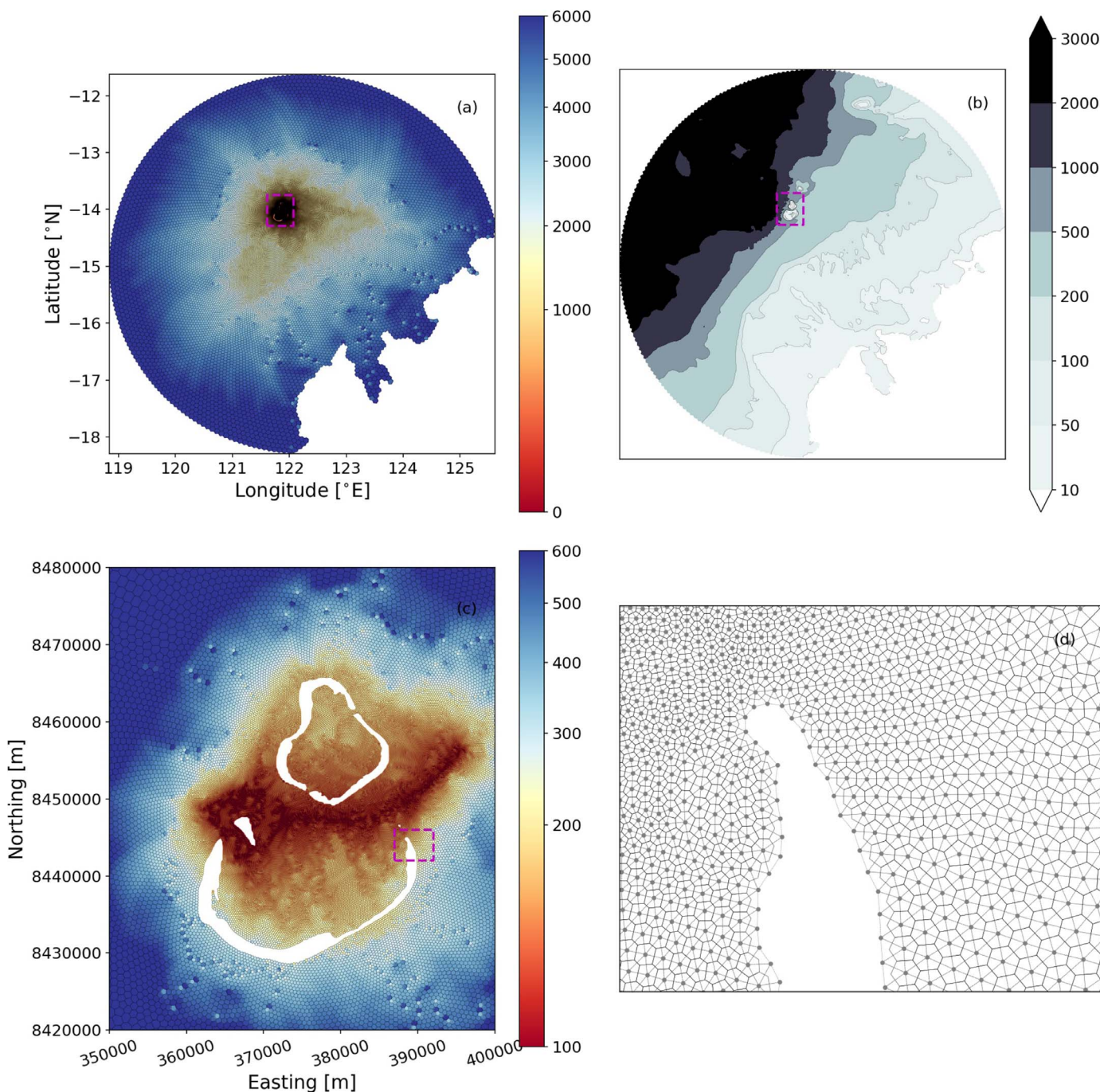
Fig. 3. (a) SUNTANS unstructured grid for the Kimberley Shelf region where the colors represent the average grid cell spacing (spacing between cell-centroids [m]), (b) model depth contours [m], (c) zoom in of the grid spacing in the region around Scott Reef indicated by the purple dashed box in (a), and (d) close-up of the hexagonal grid with the dual (triangular) grid also shown (dashed) indicated by the purple dashed box in (c). Note the different color scales between (a) and (c).

provided by Woodside Energy Ltd that spanned Scott Reef but little of the surrounding shelf. We merged the different datasets by first mapping onto the GA 250 m resolution base grid using an averaging technique to blend the scattered data onto each grid point. The 10 m and 50 m multibeam/LIDAR datasets were then merged together on the same grid by filling the 50 m multibeam data into points where there was no 10 m data. This dataset was then merged into the original GA 250 m grid by iteratively smoothing a 6.5 km buffer region where the datasets intersected.

We interpolated the merged dataset onto the SUNTANS unstructured grid using a curvature minimizing interpolation method. A simple Gaussian filter was applied to remove any grid-scale noise

introduced by the interpolation scheme. Figs. 1 and 3 b show contours of the actual model bathymetry. It is clear that the steep bathymetry around Scott Reef, with slope gradients up to 50%, was well resolved by the model. Since SUNTANS is a z-level model, it should be emphasized that little topographic smoothing was required to avoid the pressure-gradient errors endemic to sigma-coordinate ocean models.

2.3.3. Initial and boundary conditions

We are interested in the channel dynamics because it will influence the transport of tracers around the reef, however, we are also interested in the longer term transport. As the vertical density (temperature and salinity) stratification influences internal wave generation and

propagation, we tested three different background ocean state (temperature, salinity, velocity) estimates for the SUNTANS initial and boundary conditions, namely the 1/12° global HYCOM + NCODA Ocean Reanalysis (Chassignet et al., 2007), the Bluelink Reanalysis (BRAN) 2016 version (Oke et al., 2013), and the CSIRO atlas of regional seas (CARS) climatological dataset (Ridgway et al., 2002). Both HYCOM and BRAN are data-assimilating global ocean reanalysis datasets although the BRAN model is focused on the Australian region. CARS is a regional temperature and salinity climatology derived from least-squares fitting the mean plus annual and semi-annual harmonics to ocean profile observations onto a constant 3D grid. We applied a bias-correction to the CARS initial and boundary conditions by offsetting the estimate for April 2015 using temperature observations from the SCR400 mooring. Daily averaged salinity and temperature, which varied in space and time, were interpolated from each of these data sets onto the SUNTANS grid cells for use as initial and boundary conditions. Velocity data from the BRAN and HYCOM models was used to force the open boundaries only. Only salinity and temperature are available from the CARS data so boundary velocities were set to zero for this particular scenario. The initial free surface and velocity was set to zero for all cases.

Barotropic tidal velocity and free-surface boundary conditions were derived from the TPXOv7.2 global tide solution (Egbert and Erofeeva, 2002). Time-varying velocities and free-surface elevations were reconstructed from eight tidal constituents, namely M2, S2, N2, K2, K1, O1, P1, Q1, at the SUNTANS open-boundary edges. Tidal fluxes were added to the low-frequency open boundary velocities interpolated from the HYCOM and BRAN solutions.

Boundary condition data in SUNTANS is either specified as a flux along the boundary edges or by specifying the free-surface directly in the boundary cell centres. These are referred to as edge-based or cell-based open boundary types, respectively. Tracer concentrations are then specified at either cell edges or centres based on the boundary type. Edge-based boundary types are able to force meso-scale ocean features such as coastal currents at the boundary although they suffer the limitation of not allowing one to specify the free-surface directly. It is therefore difficult to maintain an equilibrium free-surface with only edge-based boundaries due to drift in the total volume of the domain. Conversely, the free-surface may be specified at cell-based boundary types but not the momentum flux. As a workaround, we used mainly edge-based boundary types for most of the domain and then used roughly ten cell-based boundaries close to the shoreline. This method allowed the free-surface to maintain a zero-mean height. We also used a sponge condition, numerically implemented as an internal momentum sink, to reduce the reflection of baroclinic waves from the boundary as described in Zhang et al. (2011).

2.3.4. Atmospheric forcing and boundary parameterisations

Atmospheric data from the ERA-Interim product provided by the European Centre for Medium Range Weather Forecast (Dee et al., 2011) was used to drive the exchange of momentum and heat between the atmosphere and the model ocean. ERA-Interim is a global, data-assimilating atmospheric hindcast model run on a roughly 100 km grid with output data stored at six-hourly time steps.

Air-sea fluxes were parameterised in SUNTANS using the COARE3.0 algorithm (Fairall and Bradley, 2003) using east- and north-wind velocity, air temperature, pressure, and relative humidity. Net longwave and shortwave radiation components were calculated internally within the model using cloud cover from the ERA-Interim data (see Rayson et al., 2015 for a description of the numerical implementation of the heat flux module into SUNTANS). A constant albedo was assumed (0.06) and the light extinction depth for shortwave radiation penetration was set spatially-constant to 20 m. A log-law drag condition was used to parameterise stress at the bottom boundary with a constant roughness length scale ($z_0 = 2 \times 10^{-3}$ m). Vertical eddy viscosity and diffusivity terms were computed using the Mellor–Yamada 2.5 turbulence closure model (Mellor and Yamada, 1982).

2.3.5. Run time

The model was setup to run for 21 days from 9 to 30 April 2015 to cover the observation period (12 to 27 April), and therefore at least one spring-neap tidal period. The first three model days spin up the surface and internal tides for the domain and were discarded. As previously mentioned, three scenarios were run with either HYCOM, BRAN, or CARS initial and boundary conditions. The model time step was 4 s. Simulations were run on 8 compute nodes of a Cray cluster, where each node has 2x 12-core Intel Xeon E5-2690 Haswell chips (192 total cores). Communication between nodes was via a Cray high-speed, low-latency Aries interconnection. Wall clock times for this configuration were roughly 18 hours for a total of 3456 CPU hours.

3. Model validation

Modeled quantities (X_{mod}) from the three different runs (HYCOM-forced, BRAN-forced, and CARS-forced) were compared against observed quanities (X_{obs}) using the root mean squared error (RMSE)

$$RMSE = \sqrt{\frac{1}{N} \sum \left[X_{obs} - X_{mod} \right]^2} \, , \tag{1}$$

bias (mean error)

$$Bias = \frac{1}{N} \sum \left(X_{mod} - X_{obs} \right), \tag{2}$$

and the Skill score (Murphy, 1988)

$$Skill = 1 - \frac{\sum \left(X_{mod} - X_{obs} \right)^2}{\sum \left(X_{obs} - \overline{X}_{obs} \right)^2}. \tag{3}$$

A Skill score of unity indicates a perfect match while anywhere between zero and one indicates that the model error is less than the observed variance. Note, the Murphy Skill score can be negative if the mean-square error is greater than the observed variance. These metrics, particularly the Skill, allow us to quantitatively determine the most suitable choice of initial and boundary condition data.

3.1. Sea surface height

Sea surface height variations at Scott Reef (site 2E) over the study period for the BRAN-forced scenario are shown in Fig. 4. Neap tides were between April 13 and 15, 2015 and peak spring tides were between April 20 and 22, 2015 when the tidal range was 4 m. Tides on the Kimberley shelf were dominated by semidiurnal components although a diurnal inequality was evident during spring tides (Fig. 4 (a)). All model runs showed good agreement between the observed sea surface heights although only the BRAN-forced scenario is shown in Fig. 4 (skill = 0.96, RMSE = 0.17 m). Spring-neap variability and phasing of the tides were all replicated by the model. The maximum error was roughly 0.3 m as shown in Fig. 4c. Free-surface predictions were largely insensitive to the initial condition because the tidal forcing was dominant.

3.2. Water temperature

Water temperature at the SCR400 mooring from the BRAN-forced model scenario and the observations are shown for the 15 day observation window in Fig. 5. Isotherm displacements peaked during spring tides with peak-to-trough amplitudes up to 100 m. A second, non-sinusoidal peak that dropped rapidly at peak flood tide, reminiscent of a transient internal hydraulic jump, was observed each tidal cycle. Higher-frequency oscillations also occurred during spring tides and were particularly apparent on the 15 and 18 °C isotherms (Fig. 5c).

Vertical displacement of the 15 °C isotherm about its mean value is shown in Fig. 6 for both the BRAN-forced model and the observations. The 15 °C isotherm was chosen as it was roughly mid-water column where the vertical displacement amplitude was largest. The model captured the phase of the two peaks during each tidal cycle, although
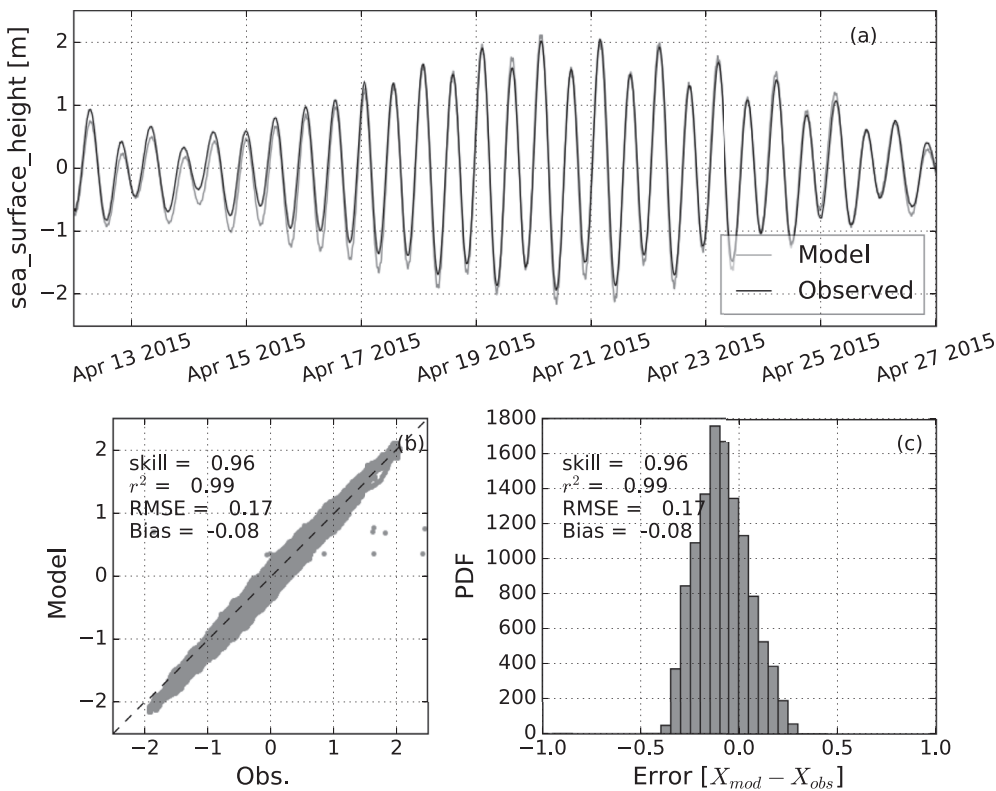
Fig. 4. (a) BRAN-forced model versus observed sea surface height at site SCR2E from 12 to 27 April 2015, (b) scatter plot, and (c) error histogram.

the model perturbations were biased towards a positive displacement while the observations showed a larger downward displacement. Differences in model and observed isotherm displacements could possibly be explained by differences in the actual background stratification (see below).

Displacement power spectral density estimates for the 15 °C isotherm are shown in Fig. 6. Peaks at the semi-diurnal forcing frequency and several higher harmonics were observed. The model captured these peaks, however, the energy between the dominant frequency bands was generally lower in the model. The slope of the spectrum for higher frequencies was similar for both the model and observations and was generally proportional to ω^{-2} (Fig. 6b). The model spectrum rolled off more sharply at frequencies beyond 6×10^{-3} s^{-1}, roughly coinciding with the horizontal wavelengths of a few horizontal grid cells i.e., the maximum wavenumber resolvable by the numerical grid.

Fig. 7 shows the temperature validation metrics in 25 m vertical bins at both SCR200 and SCR400 for all three model scenarios. The HYCOM-forced scenario performed poorest, particularly at depths greater than 150 m, with a warm bias of roughly 2 °C and the worst skill at both moorings (Fig. 7d and h). The bias-corrected CARS-forced scenario performed best with < 1 °C bias and skill > 0.5 at all depths and at both sites. The BRAN-forced scenario performed similarly to the CARS scenario except at 50–100 m depth where there was a 1.5 °C warm bias at both moorings.

3.3. Along-channel velocity

Along-channel velocity at both moorings were vertically interpolated onto fixed-depth levels for direct comparison with the model. Example time-series of the measured and the BRAN-forced modeled along-channel velocity at six depths are shown (Fig. 8). During flood tides the velocity magnitudes were up to 1.5 m s^{-1} (positive along-channel velocity) and stronger in the lower 150 m. In the upper 150 m, the magnitude was approximately half the magnitude seen in the bottom layer. There was also a phase difference between the upper and lower layers, with the peak bottom-jet layer preceding the upper layer velocity peak by about

two hours. Peak ebb (westward) velocities were not as well resolved due to mooring knockdown during this phase of the tide.

Velocity-temperature contour plots at both moorings for a four-day period during spring tides are shown in Fig. 9. The near-bed jet was not evident at the 200 m mooring, indicating it was confined to the centre region of the channel away from the wall. The strongest baroclinic shear occurred during the flood-ebb transition period when the current was negative below 100 m and positive above. Isopycnals also began upwelling during this phase of the tide. Fig. 9 shows that this process was at least qualitatively captured by the BRAN-forced model. A similar structure was also captured by the other model scenarios (not shown).

Fig. 10 shows the total (barotropic plus baroclinic) along-channel velocity validation metrics in 25 m vertical bins. The BRAN-forced scenario performed best based on all metrics. Maximum along-channel mean current at SCR400 was roughly 0.1 m s^{-1} near the bed at SCR400 and $^-$0.12 m s^{-1} near the bed at SCR200. Although the mean flow was in the same direction at the corresponding depth between the two moorings, it was roughly double in magnitude at SCR200. The BRAN-forced scenario best captured this mean profile at both sites, which was reflected by a lower bias (Fig. 7b and f at SCR200 and SCR400, respectively). Skill scores from all scenarios were largest near the bed at both sites (Skill = 0.8) and got worse towards the surface. Both HYCOM and BRAN-forced scenarios had similar RMSE and Skill scores at both sites with the latter performing slightly better. The CARS-forced scenario performed considerably poorer for all velocity comparison metrics. This suggests that other factors such as large-scale temperature gradients, not properly captured by the CARS dataset, contributed to model performance. Another possible reason is that the initial ocean state from CARS was not dynamically balanced and we gave it insufficient time to spin up. Based on these results we only consider the BRAN-forced scenario for further model analysis of the dynamics.

3.4. Harmonic analysis

Higher harmonic internal waves are generated in regions with large topographic excursion ratios (Bell, 1975; Nakamura and Awaji, 2001).
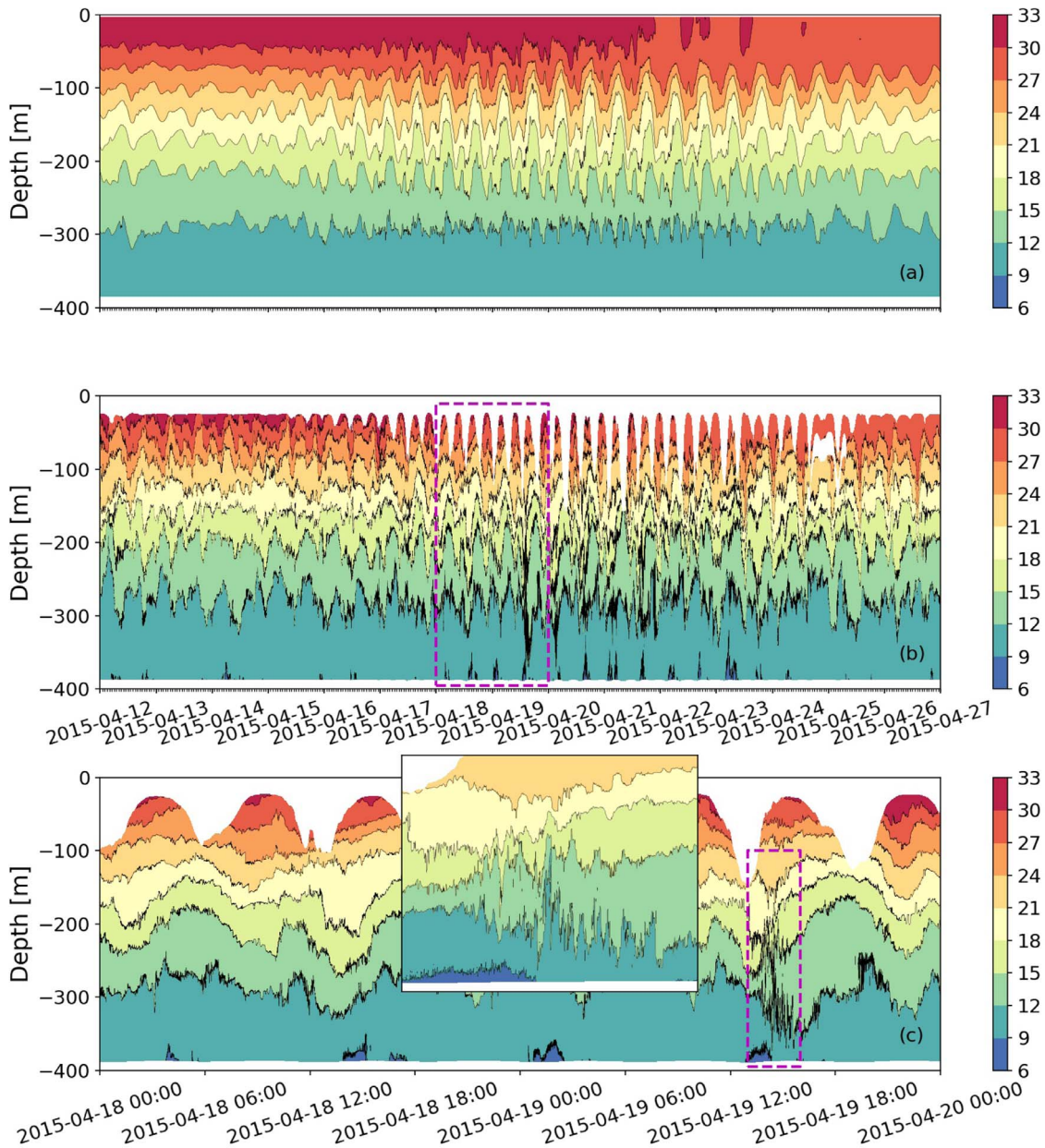
Fig. 5. Contour plot of water temperature in $z - t$ space for: (a) the BRAN-forced SUNTANS model, and (b) at the location of the SCR400 mooring and (c) zoomed in view of a two day period indicated by the purple box in (b). Isotherms are spaced at 3°C intervals. Note that the gaps at the surface are due to mooring knockdown.

We apply harmonic analysis to calculate the energy in the semidiurnal forcing frequency and its first few harmonics (M_4 and M_6) to quantify the importance of these higher frequency waves to the overall energy budget. We performed a harmonic fit on each of the model variables such that

$$\phi(x, y, z, t) = \sum_m \widehat{\phi}_m(x, y, z)\exp(-i\omega_m t) \qquad (4)$$

where ϕ is any of the model variables, e.g., u or T, and $\widehat{\phi}_m$ is the (complex) amplitude of the constituent number m. Due to the dominance of the semidiurnal tide at Scott Reef, we limit our analysis to the primary forcing frequency and its first two harmonics, i.e., M_2, M_4 and M_6 constituents during a spring-tide period (17–21 April 2015). Non-stationarity in the internal wave amplitude due to the nonlinear relationship between wave generation and tidal forcing limits the utility of harmonic decomposition over longer time periods (see e.g., Rayson, 2012). The harmonic fields then have the form

$$\phi = \begin{bmatrix} \widehat{\phi}_{M2} \\ \widehat{\phi}_{M4} \\ \widehat{\phi}_{M6} \end{bmatrix} \begin{bmatrix} e^{-i\omega t} \\ e^{-i2\omega t} \\ e^{-i3\omega t} \end{bmatrix}^T . \qquad (5)$$

The coefficient of determination, R^2, between the best-fit and the time-series from both the observations and the model was used as a metric to determine the suitability of the harmonic analysis. Here, R^2 indicates the fraction of variance explained by the harmonic fit and is given by the ratio of the variance of the harmonic signal to the original signal. The variance explained by a particular frequency is given by

$$R_n^2 = \frac{1}{2}\frac{|\widehat{\phi}_n|^2}{\langle\phi\rangle^2} , \qquad (6)$$

where $|\widehat{\phi}_n|$ is the harmonic amplitude, $\langle\phi\rangle^2$ is the input signal variance (either model or observation) and n is the frequency of choice.

Model performance was assessed using the harmonic RMSE (e.g., Rayson et al., 2011; Kang and Fringer, 2012)
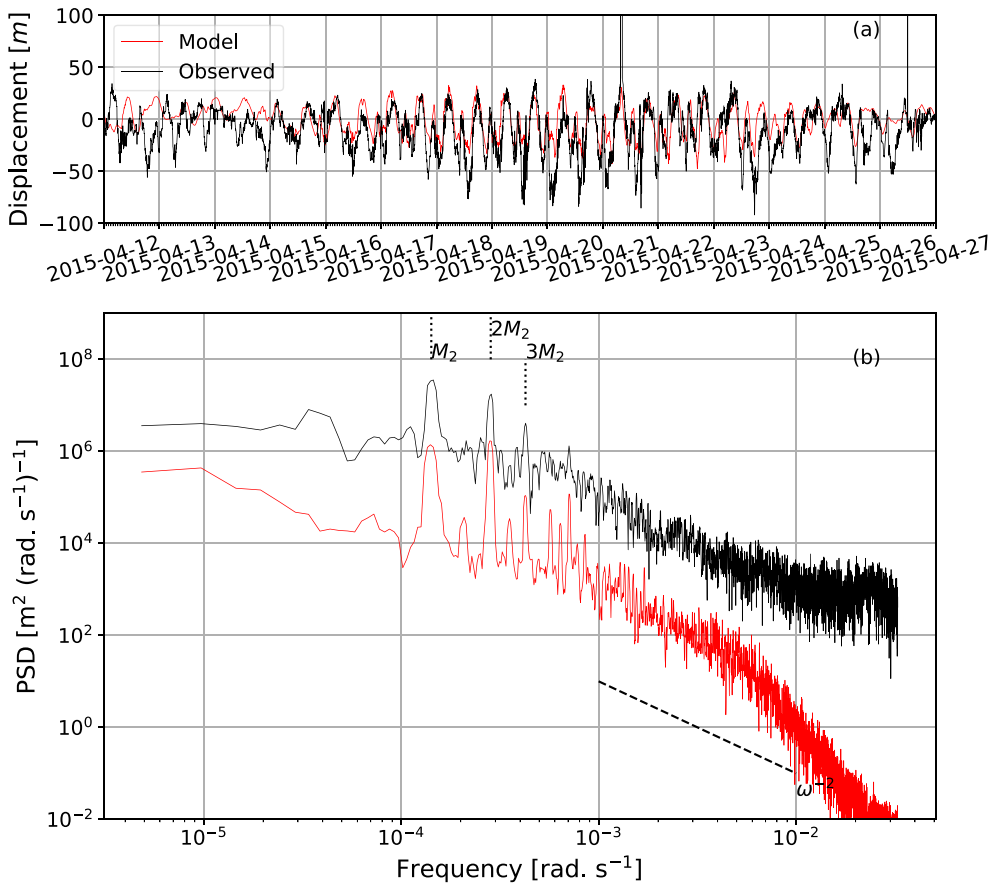
Fig. 6. (a) BRAN-forced model and observed 15 °C isotherm displacement during spring tide at the SCR400 mooring, and (b) power spectral density estimates for the corresponding displacements in (a) with the modeled spectra (grey) offset by one decade for clarity.

$$RMSE = [0.5(A_O^2 + A_M^2) - A_O A_M \cos(G_O - G_M)]^{1/2} \qquad (7)$$

where A_O and A_M are the harmonic amplitudes of the observed and modeled quantities, respectively, while G_O and G_M are the respective phase values. In order to analyse the mooring data, we mapped the velocity and temperature observations onto a fixed vertical coordinate (z-level) with 10 m spacing using linear interpolation. Temporal gaps due to mooring knockdown were then omitted from the least-squares harmonic fitting procedure. The SUNTANS data was vertically-interpolated onto the same vertical coordinate for consistency.
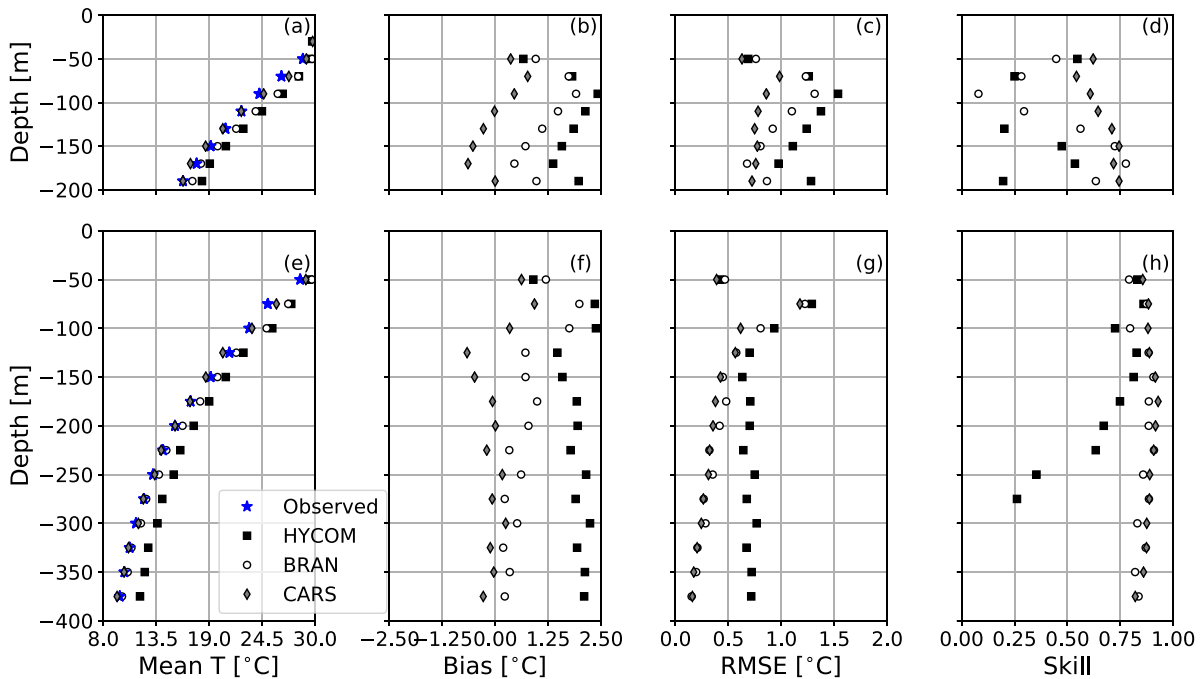

Fig. 7. Model inter-comparison for (a) mean temperature, (b) bias, (c) RMSE, and (d) Murphy skill score at SCR200. Panels (e) - (h) are the same but for the SCR400 mooring. Each SUNTANS scenario is labelled by its initial condition data source. Note the skill score in (h) goes off scale (< 0). The blue stars in (a) and (e) show the observed mean values.
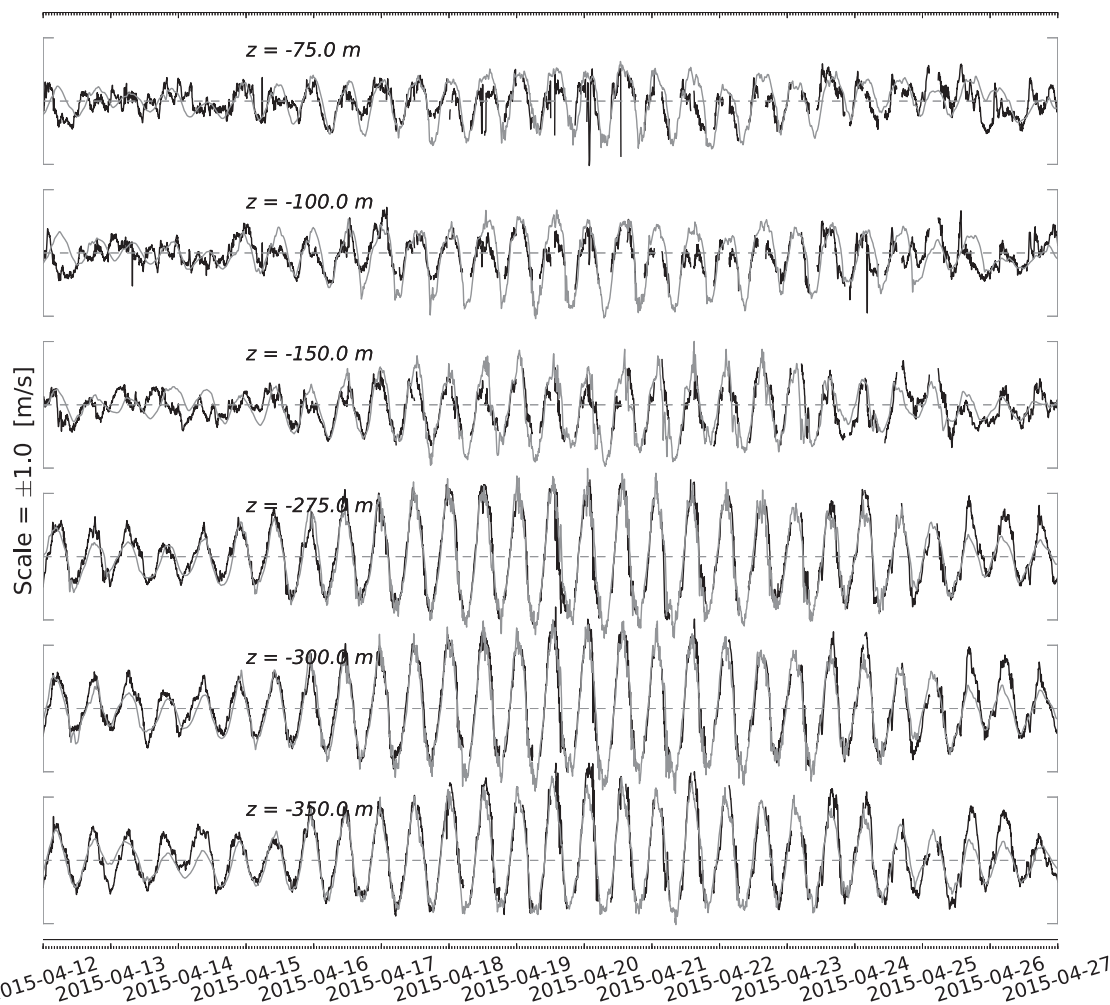
Fig. 8. Time-series of BRAN-forced model (grey) versus observed (black) along-channel velocity at six different depths at the location of the SCR400 mooring.

Examples of harmonic (tidal) semidiurnal ellipse amplitudes extracted from the 3D numerical solution are shown in Fig. 11 to highlight the effect of topography on the spatial and depth variability of the tidal currents (barotropic plus baroclinic). The magnitude of the surface semidiurnal currents peaked at roughly 1.0 m s^{-1} along the northern entrance to South Scott Reef and in the two channels into North Scott Reef. Large amplitude regions were also present along the northern and south-western flanks of the reef. The dominant semidiurnal ellipse at 300 m depth was in the channel separating North and South Scott Reef peaking at roughly 1.2 m s^{-1} (Fig. 11b). This was the region where the strong jet and high-frequency internal lee waves were observed in the mooring data.

The harmonic analysis revealed the vertical structure of the oscillatory along-channel velocity and temperature perturbations as shown in Fig. 12. There was a peak in the semi-diurnal along-channel velocity component between 200 and 350 m deep, with the model in good agreement with the observations (tidal RMSE < 0.10 m s^{-1}, Fig. 12c). The model performed worse higher in the velocity amplitude profiles (tidal RMSE 0.2–0.3 m s^{-1}) although the general shape of the profiles were similar. More than 90% of the velocity variance was explained by the harmonic fit, yet only roughly 5% of the variance was ascribed to the higher harmonics for both the observed and modeled velocity (Fig. 12b, Eq. 6). Although the M_4 frequency velocity perturbations were roughly an order of magnitude smaller than the M_2 frequency, they were similar in magnitude to the mean flow.

The observed semidiurnal temperature oscillations peaked at 1.5 °C between 75 m and 150 m below the surface (Fig. 12d). Model results

exhibited a similar vertical structure although the peak was 2.5 °C and the maximum tidal RMSE calculated using Eq. (7) was 0.8 °C at this depth (Fig. 12f). Note that more of the modeled temperature variance was captured by the harmonic fit with $R^2 = 0.95$ at 100 m depth versus $R^2 = 0.75$ for the observations (Fig. 12e). This indicates that it was likely that more of the observed temperature variance was spread in frequency bands around M_2, as is also shown in Fig. 6b. Finally, less than 50% of the temperature variance was explained by the harmonic fit in both the model and observations below 300 m depth, indicating non-oscillatory processes in that region.

Higher harmonic temperature oscillations, particularly the M_4 harmonic, were significant in the channel. M_4 frequency temperature oscillations peaked at 1.0 °C between 150 and 200 m below the surface with the model in approximate agreement (Fig. 12d). Note that almost 50% of the temperature variance, calculated using Eq. (6), was explained by the $M_4 + M_6$ harmonics in the model and 30% in the observations (Fig. 12e). The amplitudes of the M_2 and M_4 harmonics were approximately equal at 200 m depth, close to the mean depth of the 15 °C isotherm. M_6 oscillations (not shown) were generally an order of magnitude smaller.

Harmonic velocity and temperature profiles had a similar shape at the SCR200 mooring (Fig. 13). The M_4 amplitude temperature oscillations were similar in magnitude to the SCR400 mooring and peaked at 150 m below the surface. A key difference between the 200 m and 400 m mooring was a smaller peak velocity of 0.4–0.5 m s^{-1} at the SCR200 mooring. Note the bottom-intensified jet started at roughly 200 m depth at SCR400. Model error was slightly less at the 200 m mooring for both
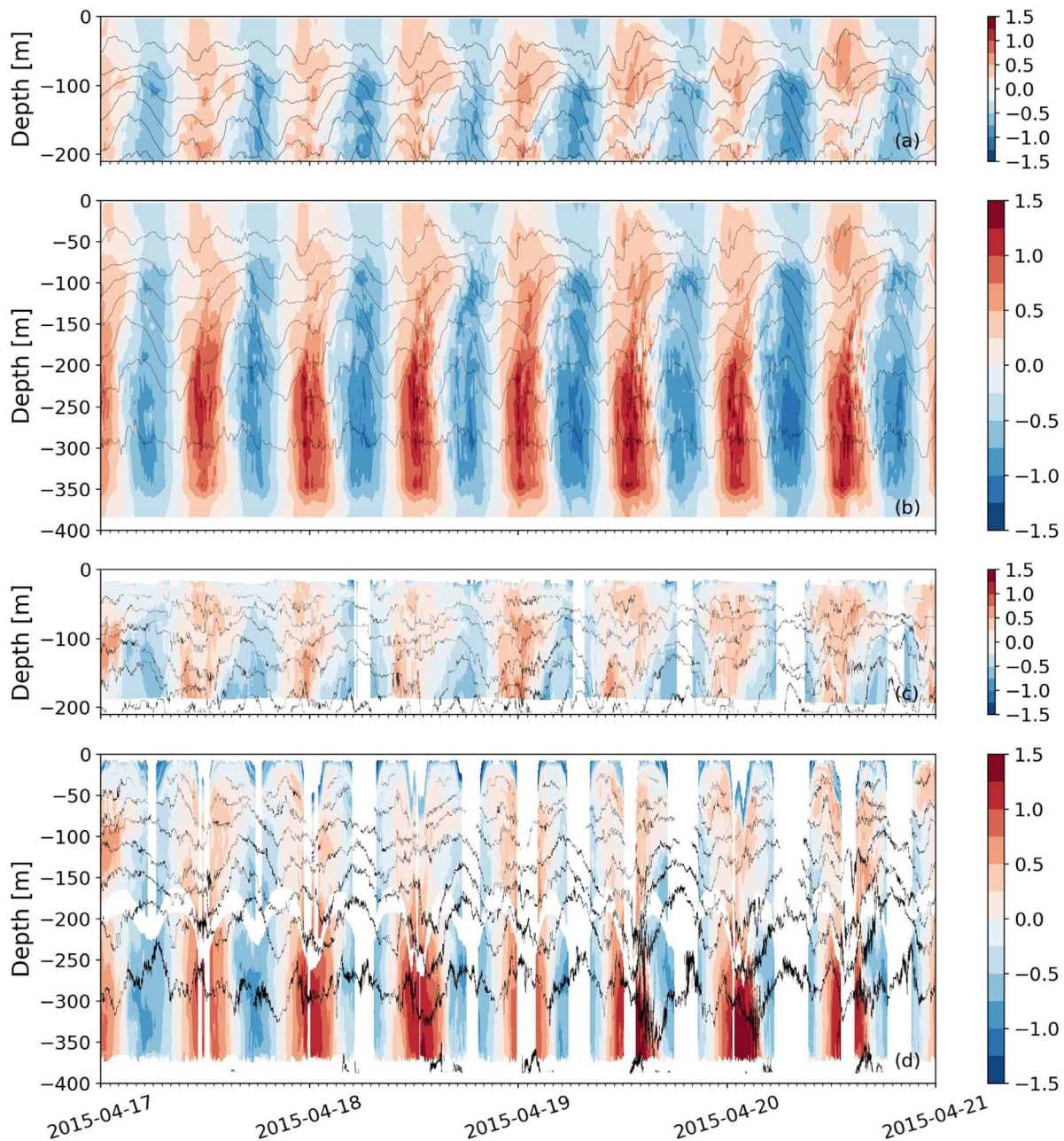
Fig. 9. Contour plot of along-channel velocity in $z - t$ space with isotherms overlaid for: (a) the BRAN-forced SUNTANS model at the location of the SCR200 mooring, and (b) for the SUNTANS model at the location of the SCR400 mooring. The respective observations are shown in (c) and (d). Isotherms are spaced at 3 °C intervals. Gaps in the velocity data are when the mooring tilt exceeded the ADCP threshold. Ebb tides are when the along-channel velocity is negative (off-shelf or westward), and vice-versa for flood tides.

harmonics of velocity and temperature (Fig. 13c and f, respectively). The M_4 frequency temperature oscillations and the bottom-intensified jet were a signature of the lee wave evolution process.

4. Internal tide dynamics in the channel

4.1. Along-channel flow

A sequence of vertical slices of the model velocity and density fields along the 400 m contour of the channel revealed the formation and evolution of tidal lee waves into a transient internal hydraulic jump over one tidal cycle (Fig. 14). The upper panel shows a time-series at the SCR400 mooring to place the vertical slices in the context of Fig. 9b. During the flood phase, the channel shape forced an increase in the horizontal velocity in the convergent section (easting 378 km) and a

decrease in the divergent section (easting 383 km) of the channel (Figure 14 b, c). In the main convergent section (easting 378 - 383 km), the flow accelerated and the isopycnals between 150 and 300 m depth were drawn down, while below 300 m the isopycnals were displaced upwards, thus creating a mode-two vertical structure. The mode-two internal Froude number transitioned from super- to sub-critical in this region during this stage of the tide, indicating likely trapping of mode-two internal waves (Fig. 2d). The along-channel velocity was greatest in this section and the vertical profile defined the bottom-intensified jet observed at the SCR400 mooring. In the divergent section of the channel between easting 383 and 385 km, the flow then decelerated and the isopycnals returned sharply to their mean position as an internal hydraulic jump (Fig. 14d, e). The local vertical displacement of the isopycnals was approximately 50 m and the horizontal length scale of this jump feature was approximately 4 km. Vertical shear was
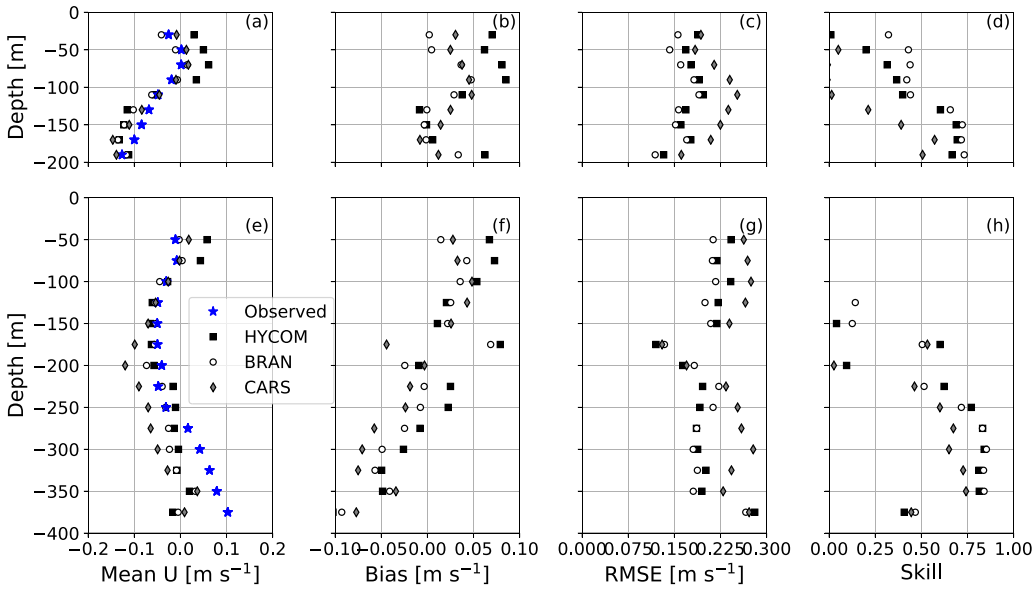
Fig. 10. As in Fig. 7 but for the total along-channel (eastward) velocity component. Skill scores above -100 m in (h) are off-scale.

greatest at the mooring location during the flood-ebb transition phase as the transient jump began to propagate back into the channel (Fig. 14e, f). Observations indicated that internal wave breaking, indicated by large amplitude isopycnal overturns, also occurred at this site during this phase of the tide (see Fig. 5c).

Similar to the response at the eastern-end of the channel during flood tide, a jump formed at the western-end of the channel during ebb tide (Fig. 14h at easting 375 km). This jump was located higher in the water column (50–300 m) than the jump at the eastern end. The differences in the flow response at the eastern and western ends of the channel were likely due to the asymmetry in the variation of width and depth either side of the point of maximum contraction (see Fig. 2b). At SCR400, for example, high vertical shear did not occur on the ebb-flood phase like it did on the flood-ebb phase.

4.2. Energetics

We used the harmonically-decomposed velocity and density fields to calculate the baroclinic energy density E [J m^{-2}], at both the forcing

frequency (M_2) and at the first two harmonics (M_4, M_6). Using a similar method to that outlined in Rayson et al. (2012), the time-averaged, depth-integrated internal wave energy density in harmonic form is

$$E_m = \langle \overline{E_{k,m}} \rangle + \langle \overline{E_{p,m}} \rangle, \tag{8}$$

where

$$\langle \overline{E_{k,m}} \rangle = \Re\left\{ \frac{\rho_0}{4} \int_{-H}^{0} \widehat{u'}_m^2 + \widehat{v'}_m^2 + \widehat{w'}_m^2 \, dz \right\} \tag{9}$$

is the kinetic energy at frequency m, $\widehat{u'}_m$, $\widehat{v'}_m$, $\widehat{w'}_m$ are the complex harmonic amplitudes of each baroclinic velocity component, an overbar indicates depth-integration, and the angle brackets indicate a time-average operator.

$$\langle \overline{E_{p,m}} \rangle = \Re\left\{ \frac{\rho_0}{4} \int_{-H}^{0} \frac{\hat{b}_m^2}{N^2} \, dz \right\} \tag{10}$$

is the linear available potential energy at a particular harmonic (APE_3 using the definition of Kang and Fringer (2010)), $\hat{b}_m = \widehat{\rho'}_m g / \rho_0$ is the
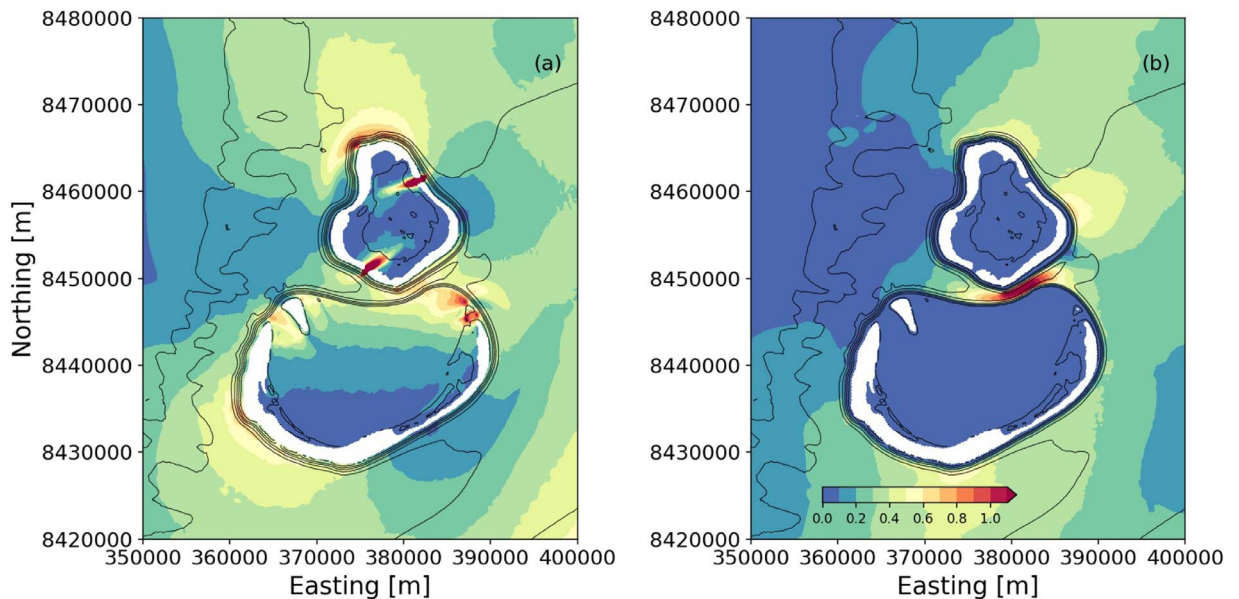

Fig. 11. Semi-diurnal (M_2) major tidal ellipse amplitude [m s^{-1}] at (a) the surface, and (b) 300 m below the surface.
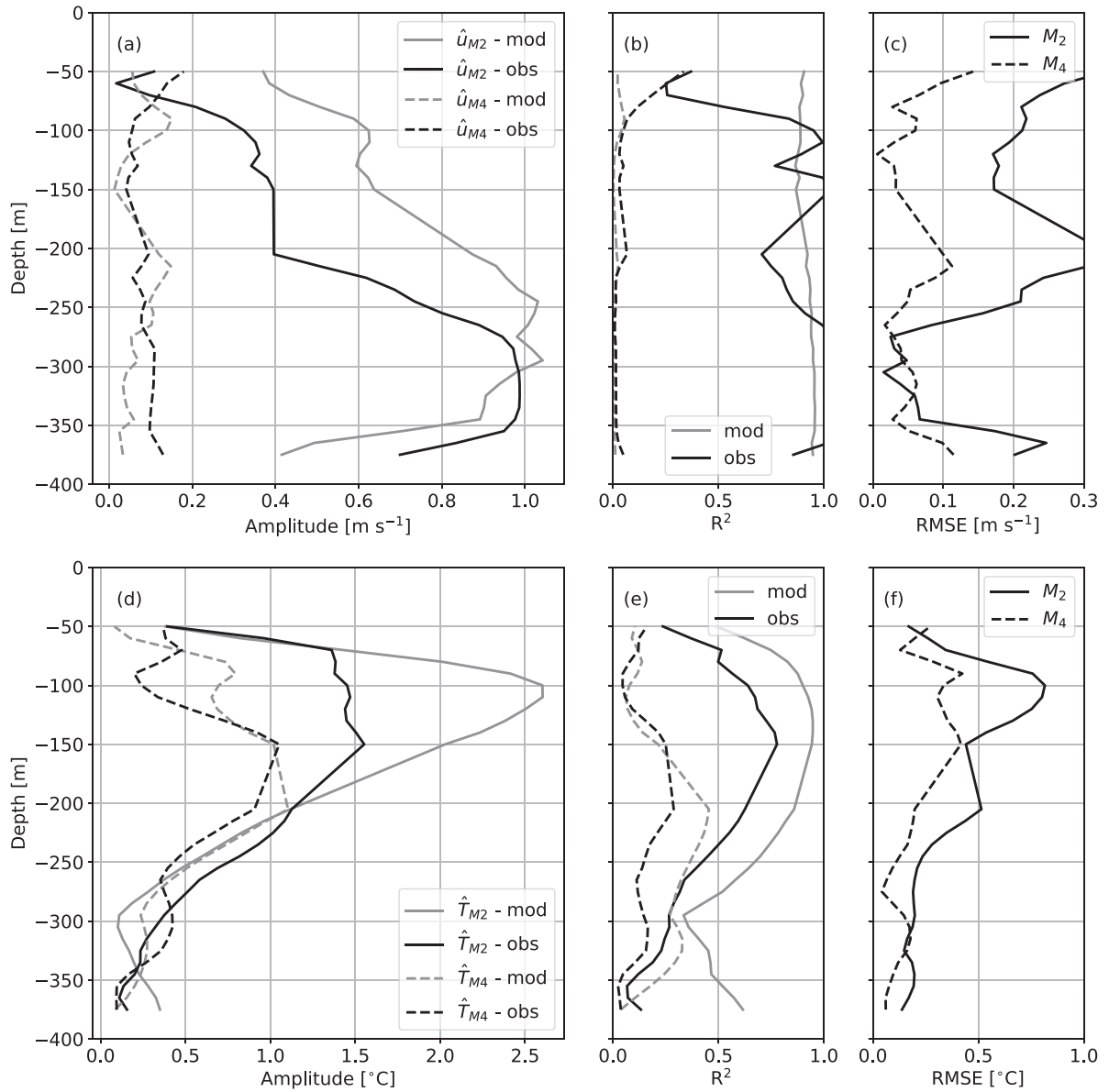
Fig. 12. (a) M_2 and M_4 harmonic along-channel velocity amplitude, (b) harmonic fit coefficient of determination (R^2), and (c) harmonic RMSE from Eq. (7) at the SCR400 mooring. (d), (e), and (f) show the same as (a), (b) and (c) but for temperature. The dashed black and grey lines in (b) and (e) indicate the fraction of variance explained by the $M_4 + M_6$ harmonics only (Eq. (6)).

buoyancy perturbation at the harmonic, and N is the buoyancy frequency. The baroclinic energy flux vector is then

$$\langle \overline{\mathbf{F}_m} \rangle = \Re \left\{ \frac{\rho_0}{2} \int_{-H}^{0} \widehat{\mathbf{u}'}_m p_m^* \, dz \right\} \quad [\text{W m}^{-1}] \tag{11}$$

where $\widehat{\mathbf{u}'}_m = \widehat{\mathbf{u}_m} - \widehat{\mathbf{u}}$ is the complex baroclinic velocity, and $p_m^* = \int_z^0 \hat{b}_m \, dz'$ is the complex conjugate of the baroclinic pressure perturbation. The barotropic velocity amplitude, $\widehat{\mathbf{u}}$, was calculated by depth-averaging the total velocity amplitude.

The steady-state, tidally-averaged baroclinic kinetic energy equation in harmonic form is

$$\nabla_H \cdot \langle \overline{\mathbf{F}_m} \rangle + NL_{mn} = C_m + DISS_{mn} \tag{12}$$

where $\nabla_H \equiv (\partial/\partial x, \partial/\partial y)$, C_m is the barotropic to baroclinic conversion,

$$C_m = \Re \left\{ -\frac{1}{2} (\widehat{\mathbf{u}}_m \cdot \nabla H) p_m^*(-H) \right\}, \tag{13}$$

NL_{mn} are the nonlinear advection terms and $DISS_{mn}$ are the dissipation terms. The nonlinear and dissipative terms in the internal wave energy

equation are presented in Kang and Fringer (2012) and it is beyond the scope of this paper to derive their harmonic equivalents. Time-dependent residual terms arise after time-averaging the flux and conversion terms when two frequencies interact that are non-integer multiples of one another, i.e., non-harmonic tidal constituents such as M_2 and K_1. Energy transfer between different harmonics, indicated by the mn subscript, only occur in the nonlinear and dissipative terms. We approximate the forcing in this region as a single semidiurnal frequency so that we may assume steady state, which is only reasonable for periods of several days, beyond which the contributions from other frequencies are important. The purpose here is to show that there was a significant contribution to the energy flux divergence from the higher harmonics that was linked to the tidal lee wave evolution.

We calculate the energy terms in Eqs. (9) and (11) for the mooring data using the harmonic velocity and temperature terms from Section (3.4). Vertical integrals were computed by extrapolating the closest velocity and temperature perturbations to the surface and seabed, respectively. A nonlinear equation of state using constant salinity (34.6 psu) was used to convert observed temperature to buoyancy
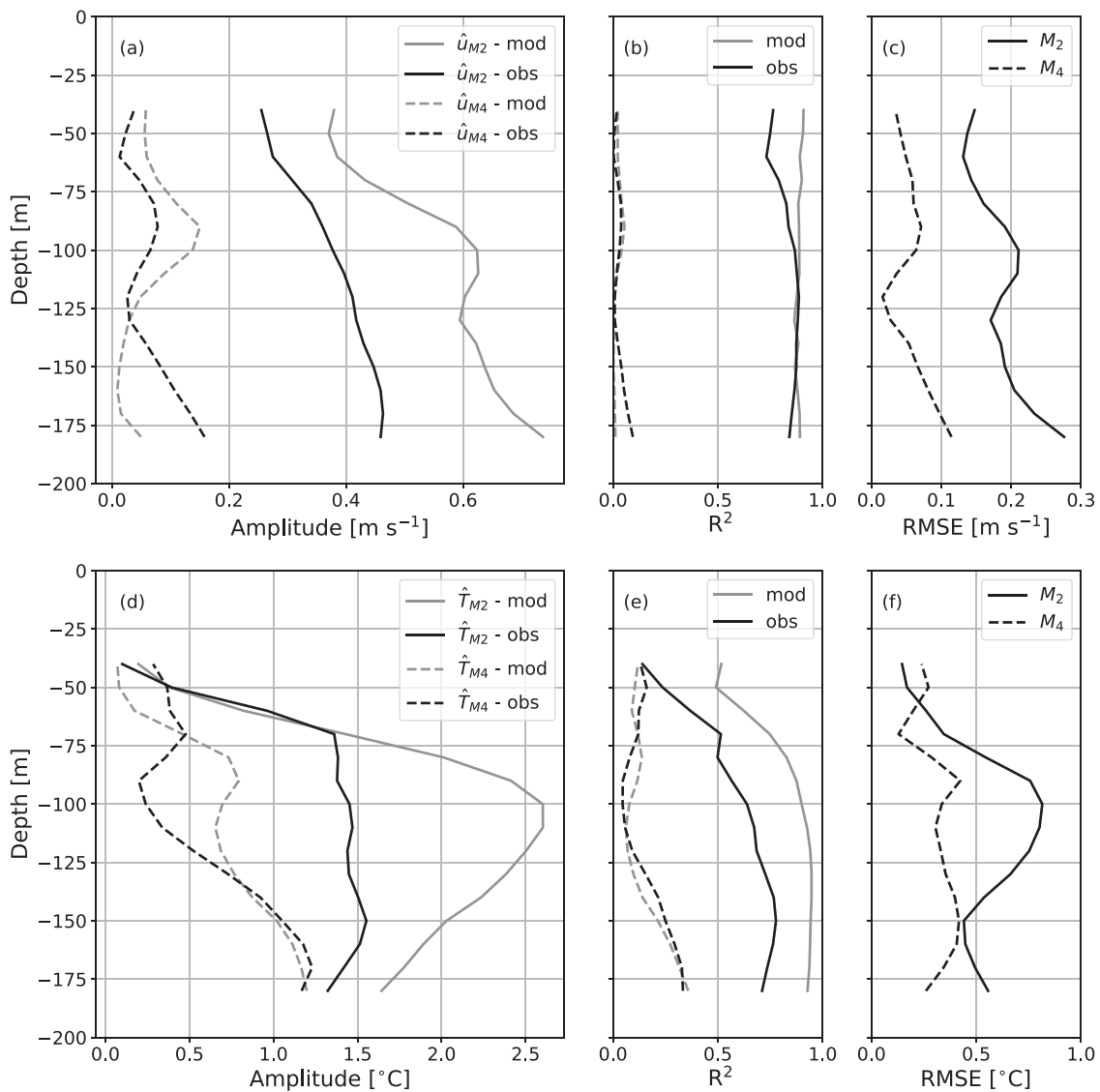
Fig. 13. As in Fig. 12 but for the SCR200 mooring.

perturbations. Both observed and model energy quantities were computed on the same vertical grid for consistency.

Depth-integrated energy density (Eq. 9) and the eastward energy flux (Eq. 11) at the SCR400 mooring are listed in Table 1. The semidiurnal model total energy density was roughly 35% less than observed, although both were of order 10 kJ m^{-2}. The M_4 frequency energy was roughly three times smaller in the model than the observations, and both the model and observed energy densities were around an order of magnitude less than the semidiurnal component. Observed semidiurnal eastward (along-channel) energy fluxes were roughly $^-11$ kW m^{-1} and the model captured the direction, although it was 15% weaker than the observations. The M_4 flux component was in poorer agreement. The sign was opposite, although as we show below, there was considerable spatial variability in the M_4 flux divergence in this section of the channel where the moorings were located meaning that a small change in position could change the sign of the M_4 energy flux.

The M_2 component energy density was larger in the model at the SCR200 mooring (4550 and 2020 J m^{-2} for the model and observations, respectively). The M_4 component was still roughly twice as energetic in the observations. Eastward M_2 fluxes were significantly weaker than at the SCR400 mooring with modeled and observed components of $^-3$ and $^-1.5$ kW m^{-1}, respectively. While uncertainties in the energy and flux estimates due to depth and time gaps may contribute to some error, the

model appeared to capture the direction, magnitude and relative contributions from higher harmonics at this site.

Spatial variation of the internal wave energy density with flux vectors overlaid for the forcing frequency and its first harmonic are shown in Fig. 15. The largest semidiurnal energy density was 15–20 kJ m^{-2} in the main section of the channel and along the southern flank of Scott Reef (Fig. 15a). The M_4 energy density was roughly five times smaller than the main forcing frequency (Fig. 15b). The area-averaged M_2 and M_4 energy density was 4.8 and 0.9 kJ m^{-2}, respectively. There was, however, higher intensity M_4 peaks of 2 kJ m^{-2} at either end of the channel, i.e., at easting 370–378 and 383–390 km. This coincided with the regions where tidal lee waves formed and propagated back into the channel (Fig. 14d).

The horizontal energy flux divergence from Eq. (12) is shown for the channel region in Fig. 16 and area-integrated flux divergence and barotropic to baroclinic conversion (Eq. 13) are shown in Table 2. The M_2 frequency flux vectors were divergent along the southern flank, indicating wave generation, and convergent within the channel (indicated by a negative sign). The channel separating North and Scott Reef was a region of net M_2 energy convergence ($^-2.7$ MW) and net M_4 divergence (6.5 MW). Net barotropic to baroclinic conversion rates in the corresponding region were 15 and $^-0.6$ MW for the M_2 and M_4 frequencies, respectively. M_2 frequency internal tide energy was
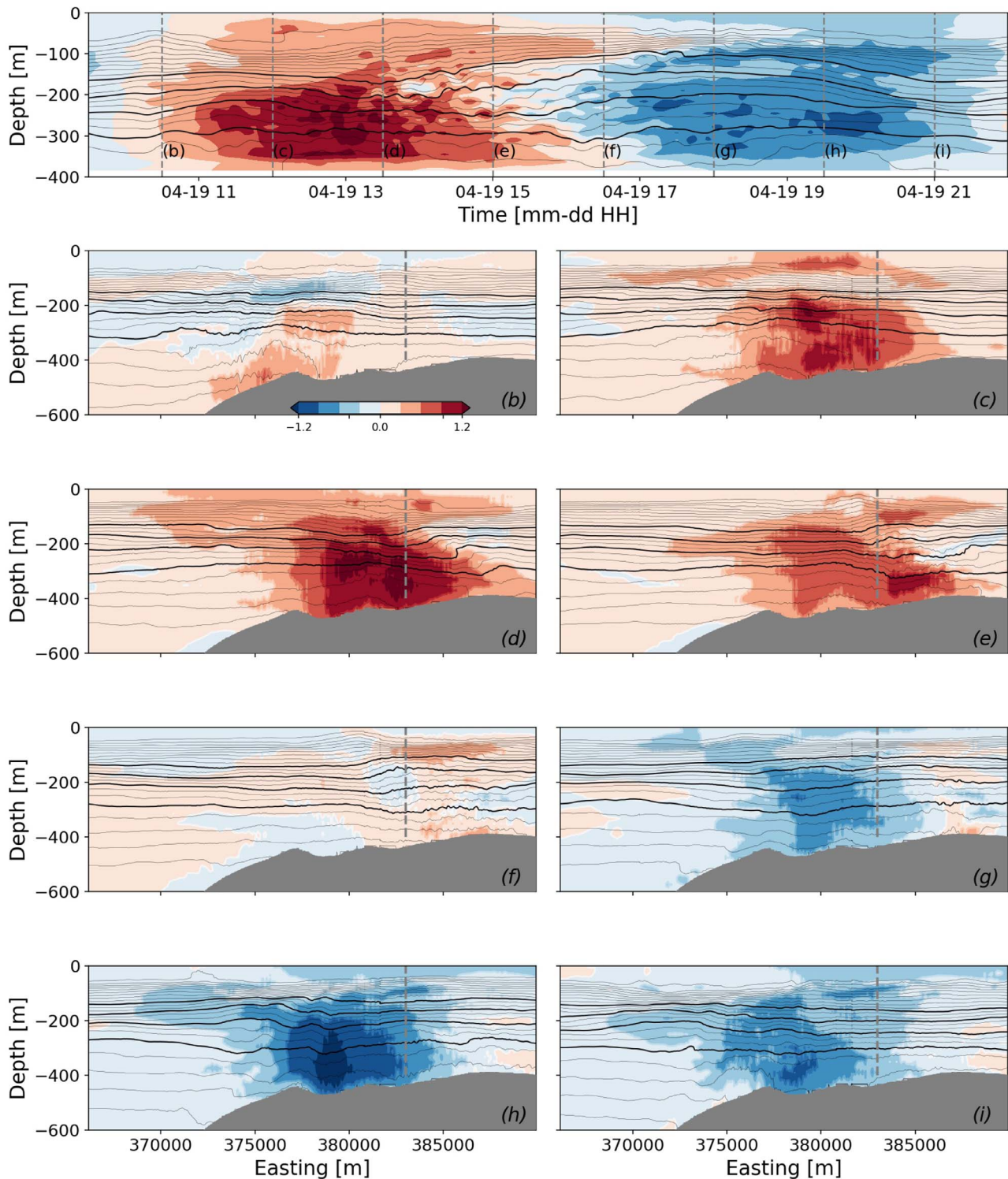
Fig. 14. (Top panel) Time-series at the SCR400 mooring location from the model over a typical (Spring) tidal cycle. (b) - (i) Model vertical slices of temperature and eastward velocity [m s^{-1}] along the channel *thalweg* with the velocity color scale in panel (b). Snapshots start at peak flood tide and sequence at time intervals indicated by the vertical dashed lines in (a) through an M_2 tidal cycle. Isotherms are spaced at 1 (thin) and 3 (thick) °C intervals. The vertical dashed lines in (b)–(i) indicate the mooring location.

therefore being lost in the channel and little of the converted energy was leaving the region. As the M_4 divergence greatly exceeded the conversion we conclude that some of the energy at this harmonic was transferred directly from the forcing frequency via nonlinear interactions, i.e., advection of waves by barotropic or baroclinic currents.

Note that spurious M_4 energy can arise due to the tidal advection of freely propagating waves observed in an Eulerian frame (see e.g., Pinkel, 2008; Stephenson et al., 2016). Stephenson et al. (2016) show

that harmonic filtering under-predicts the primary frequency (M_2) amplitude of a low-mode internal wave subject to a maximum internal Froude number of 0.5 by 20–30%; the first harmonic (M_4) is over-predicts by a corresponding amount. If tidal advection is important ($Fr_n > 1$) then a Lagrangian analysis of the harmonics is necessary to separate the freely propagating waves from the advected signal (e.g., Musgrave et al., 2016; Nagai et al., 2015; Shakespeare and Hogg, 2017). This method would be necessary to exactly balance an internal

Table 1

Depth-integrated energy density and eastward energy flux at the SCR400 and SCR200 moorings for the M_2 and M_4 frequency. Both the modeled (Mod.) and observed (Obs.) quantities are listed.

Energy Term	SCR400 M_2	SCR400 M_4	SCR200 M_2	SCR200 M_4
E_m - Mod. [J m^{-2}]	8740	560	4550	440
E_m - Obs. [J m^{-2}]	13230	1590	2023	890
$F_{m,x}$ - Mod. [W m^{-1}]	−9580	−290	−2960	−170
$F_{m,x}$ - Obs. [W m^{-1}]	−11070	1030	−1450	520

tide energy equation in frequency form. However, based on the past studies with a similar vertical wavenumber and Froude number parameter space, we expect that tidal advection will only modify the total M_4 energy density by a small amount. Furthermore, given the M_4 signal was 5–10 times more energetic in the channel we conclude that this was predominantly the result of tidal lee waves.

5. Discussion

A number of the flow features observed and captured by the 3D model were qualitatively similar to flows over two-dimensional sills (e.g., Klymak et al., 2010; Winters and Armi, 2013). For a 2D sill, part of the flow is blocked below the crest and a fast flowing layer or jet forms above the crest to compensate for this blockage at depth. The blocked layer depth is proportional to U_0/N (Gill, 1982; Baines, 1995). Both steady (Klymak et al., 2010) and unsteady (Winters and Armi, 2013) 2D numerical simulations show that a bottom-intensified jet forms in the initial lee wave development stage close to the topographic crest. Klymak et al. (2010) show that the vertical scale of the jet increases with the topographic Froude number, $Fr_t = Nh_m/U_0$, where h_m is the obstacle height. Therefore low-mode lee waves form when the topographic height is much larger than the blocking depth. At Scott Reef, the jet height or thickness was roughly 150 m and the wave response is considered to be low-mode (mode one or two). But as the flow was controlled by a contraction, it is difficult to define an equivalent scale to h_m to compare with the 2D case.

In a contraction with no sill, or other three-dimensional topography, only part of the flow is blocked close to the channel edges yet the flow
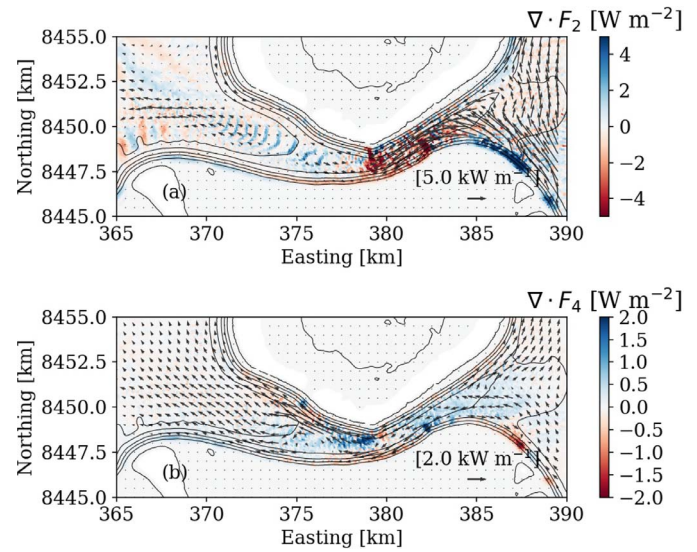

Fig. 16. Depth-integrated internal wave flux divergence [W m^{-2}] for (a) the M_2, and (b) the M_4 frequency. Energy flux vectors at each frequency are also overlaid.

Table 2

Area-averaged harmonic energy density, area-integrated flux divergence and barotropic to baroclinic conversion terms for the Scott Reef channel region roughly indicated by Fig. 2(a).

	M_2	M_4	M_6
$\langle \overline{E_{p,m}} \rangle$ [J m^{-2}]	1730	730	80
$\langle \overline{E_{k,m}} \rangle$ [J m^{-2}]	2140	370	70
$\nabla_H \cdot \langle \overline{F_m} \rangle$ [MW]	−2.7	6.5	0.5
C_{mn} [MW]	15.1	-0.6	0.0

along the *thalweg* is unimpeded by topography. It is this effective blocking near the sloped walls causing the flow to be deflected toward the *thalweg* instead of going up slope that likely causes the near-bed jet. This is the dividing-streamline concept in 3D flows (see e.g., Castro et al., 1983; Snyder et al., 1985). Castro et al. (1983) (and others) show that for a steady, adiabatic flow the position of the dividing-streamline
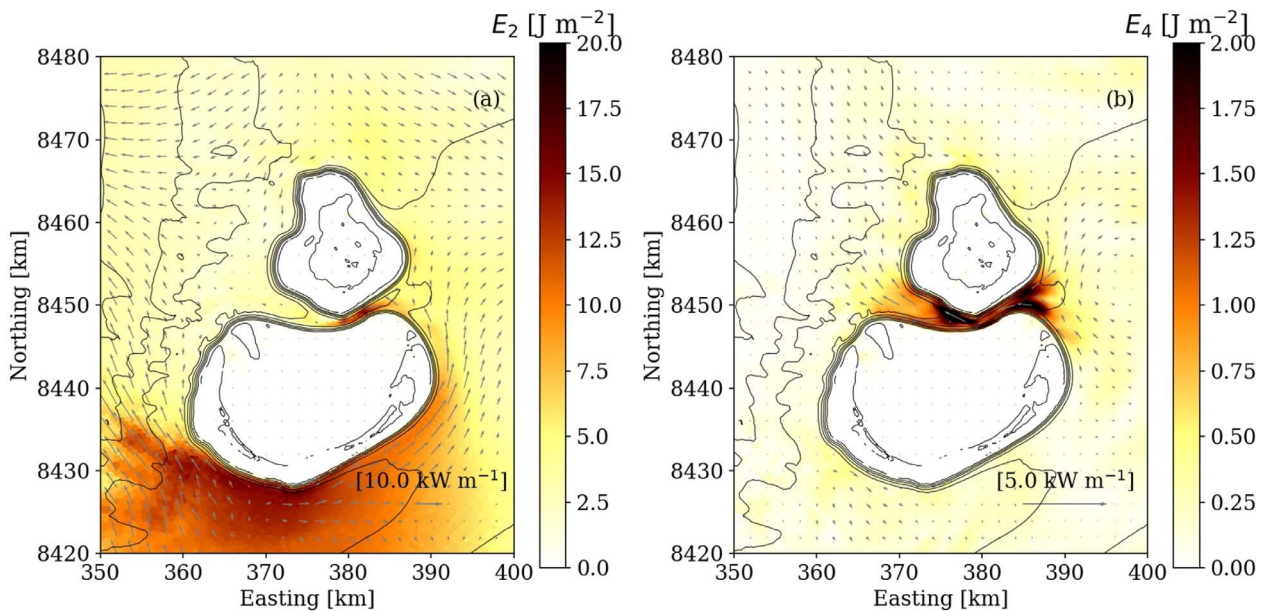

Fig. 15. Depth-integrated internal wave energy density [kJ m^{-2}] for: (a) the M_2, and (b) the M_4 frequency. Energy flux vectors at each frequency are also overlaid. Note the difference in color and vector scales between (a) and (b).

can be calculated based on energy conservation. Layers where the flow has insufficient kinetic energy to overcome the potential energy necessary to lift the fluid over the topography will instead deflect around the topography and form a jet. Castro et al. (1983) show experimentally that lee waves and overturns then form downstream, qualitatively similar to our observations. Although the dividing-streamline conceptually explains the formation of the bottom jet at Scott Reef, idealised modeling is necessary to determine the dependence of the jet height (internal wave mode) on the topographic geometry as well as the effects of unsteady forcing and turbulent dissipation that are important in the present application.

6. Summary and conclusions

We have demonstrated how high-frequency internal lee waves were generated at steep island topography using a z-level, unstructured grid RANS model driven by realistic forcing and validated using ocean mooring observations. The focus was on a spring-neap tidal period in April 2015 when moored observations were collected, although the model could potentially be used for longer-term predictions as it was one-way nested within different global circulation models (or climatological datasets), as well as the TPXO tidal model and surface heat and momentum fluxes specified from a global atmospheric reanalysis model (ERA-Interim). A hex-dominant unstructured mesh was used to resolve the island topography down to 100 m scale while alleviating the horizontal divergence calculation errors associated with triangular Arakawa-C grid finite-volume models (see e.g., Wolfram and Fringer, 2013). The z-level vertical discretization was necessary due to the very steep island atoll bathymetry with bottom slopes of up to 50 %.

We compared three different scenarios, each forced with different initial and boundary conditions, and concluded that the BRAN-forced scenario performed best in terms of all validation metrics for both water temperature and along-channel velocity. This scenario had a lower temperature bias than the HYCOM-forced scenario in this region and captured the velocity variability better than a scenario initialized with the CARS climatological data. The BRAN-forced scenario was weakest at about the 100 m depth in the peak thermocline region, with a 1.5 °C bias. Inaccurate description of mixing in the thermocline driven by internal tide-induced processes was possibly a cause of the bias in both global models as they do not include tides and are too coarse to resolve the internal tides in detail. Insufficient observational coverage in the region was also a challenge.

Observations revealed an oscillatory bottom-intensified jet, intensifying with the tidal forcing amplitude, in the 500 m deep channel separating the two reef atolls. Isotherm oscillations at twice the dominant semidiurnal forcing frequency were observed in the same region, in addition to the longer wave length internal tide. Our model was able to capture these dominant and key flow features in the channel. The 3D model revealed that M_4 (and higher) frequency oscillations were formed in the lee of a transient hydraulic jump in the divergent section of the channel (see Fig. 14). We interpret these high-frequency oscillations as topographic lee waves. An energetics analysis of the model output revealed a net convergence of internal tide (M_2 frequency) energy in the channel, and a net divergence of higher frequency energy. Based on the harmonic energy density calculated from both the observations and the model (Table 1), roughly 10% of the internal tide energy was transferred to higher frequencies, in particular the M_4 frequency. This energy transfer is a direct mechanism for energy cascade to higher harmonics with shorter wave lengths that were steeper and therefore more likely to break.

The observations indicated the topographic lee waves eventually broke on the turn of the tide, leading to large scale overturning events (see e.g., Fig. 5c around 2015-04-19 12:00). The grid scale required to capture this breaking process was beyond the resolution of our RANS model, although the model was able to reproduce the larger-scale conditions that led to these events, i.e., the tidal lee wave formation. In

a follow up study, we will examine the observed dissipation and vertical mixing rates associated with these breaking events and use the model developed here as a tool to ascertain the importance of these events for vertical heat and nutrient fluxes in the region.

References

Alford, M.H., Klymak, J.M., Carter, G.S., 2014. Breaking internal lee waves at Kaena Ridge, Hawaii. Geophys. Res. Lett. 41 (3), 906–912.

Baines, P.G., 1995. Topographic Effects in Stratified Flows. Cambridge University Press, Cambridge.

Bell, T.H., 1975. Lee Waves in Stratified Flows with Simple Harmonic Time-Dependence. J. Fluid Mech. 67 (Feb25), 705–722.

Buijsman, M.C., Legg, S., Klymak, J., 2012. Double ridge internal tide interference and its effect on dissipation in Luzon Strait. J. Phys. Oceanogr. 42 (8), 1337–1356.

Castro, I., Snyder, W., Marsh, G., 1983. Stratified flow over three-dimensional ridges. J. Fluid Mech. 135, 261–282.

Chassignet, E.P., Hurlburt, H.E., Smedstad, O.M., Halliwell, G.R., Hogan, P.J., Wallcraft, A.J., Baraille, R., Bleck, R., 2007. The HYCOM (HYbrid Coordinate Ocean Model) data assimilative system. J. Mar. Syst. 65 (1-4), 60–83. http://tds.hycom.org/thredds/dodsC/GLBu0.08/expt_19.1/3hrly.html.

Collins, L.B., Testa, V., 2010. Quaternary development of resilient reefs on the subsiding Kimberley continental margin, northwest Australia. Braz. J. Oceanogr. 58, 67–77.

Dee, D.P., Uppala, S.M., Simmons, A.J., Berrisford, P., Poli, P., Kobayashi, S., Andrae, U., Balmaseda, M.A., Balsamo, G., Bauer, P., Bechtold, P., Beljaars, A.C.M., van de Berg, L., Bidlot, J., Bormann, N., Delsol, C., Dragani, R., Fuentes, M., Geer, A.J., Haimberger, L., Healy, S.B., Hersbach, H., Holm, E.V., Isaksen, L., Kollberg, P., Kohler, M., Matricardi, M., Mcnally, A.P., Monge-Sanz, B.M., Morcrette, J.J., Park, B.K., Peubey, C., de Rosnay, P., Tavolato, C., Th??paut, J.N., Vitart, F., 2011. The ERA-Interim reanalysis: configuration and performance of the data assimilation system. Q. J. R. Meteorol. Soc. 137 (656), 553–597.

Edwards, K.a., MacCready, P., Moum, J.N., Pawlak, G., Klymak, J.M., Perlin, A., 2004. Form drag and mixing due to tidal flow past a sharp point. J. Phys. Oceanogr. 34 (6), 1297–1312.

Egbert, G., Erofeeva, S., 2002. Efficient inverse modeling of barotropic ocean tides. J. Atmosp. Oceanic Technol. 19, 183–204. http://volkov.oce.orst.edu/tides/global.html.

Fairall, C., Bradley, E., 2003. Bulk parameterization of airsea fluxes: updates and verification for the COARE algorithm. J. Clim. 571–591.

Fringer, O.B., Gerritsen, M., Street, R.L., 2006. An unstructured-grid, finite-volume, nonhydrostatic, parallel coastal ocean simulator. Ocean Model.(October) 1–55.

Gill, A. E., 1982. Atmosphere - Ocean Dynamics.

Gilmour, J.P., Smith, L.D., Heyward, A.J., Baird, A.H., Pratchett, M.S., 2013. Recovery of an isolated coral reef system following severe disturbance. Science 340 (6128), 69–71.

Gove, J.M., McManus, M.a., Neuheimer, A.B., Polovina, J.J., Drazen, J.C., Smith, C.R., Merrifield, M.a., Friedlander, A.M., Ehses, J.S., Young, C., Dillon, A.K., Williams, G.J., 2016. Near-island biological hotspots in barren ocean basins. Nat. Commun. 7, 1–34.

Holleman, R.C., Fringer, O.B., Stacey, M., 2013. Numerical diffusion for flow aligned unstructured grids with application to estuarine modeling. Int. J. Numer. Methods Fluids 72 (February), 1117–1145.

Hughes, T.P., Kerry, J.T., Álvarez-Noriega, M., Álvarez-Romero, J.G., Anderson, K.D., Baird, A.H., Babcock, R.C., Beger, M., Bellwood, D.R., Berkelmans, R., et al., 2017. Global warming and recurrent mass bleaching of corals. Nature 543 (7645), 373–377.

Kang, D., Fringer, O., 2010. On the calculation of available potential energy in internal wave fields. J. Phys. Oceanogr. 40 (11), 2539–2545.

Kang, D., Fringer, O., 2012. Energetics of barotropic and baroclinic tides in the monterey bay area. J. Phys. Oceanogr. 42 (2), 272–290.

Klymak, J.M., Legg, S.M., Pinkel, R., 2010. High-mode stationary waves in stratified flow over large obstacles. J. Fluid Mech. 644, 321.

Legg, S., Klymak, J., 2008. Internal hydraulic jumps and overturning generated by tidal flow over a tall steep ridge. J. Phys. Oceanogr. 38, 1949–1964.

Mellor, G.L., Yamada, T., 1982. Development of a turbulence closure model for geophysical fluid problems. Rev. Geophys. 20 (4), 851–875.

Murphy, A., 1988. Skill scores based on the mean square error and their relationships to the correlation coefficient. Mon. Weather Rev 116, 2417–2424.

Musgrave, R., Mackinnon, J., Pinkel, R., Waterhouse, A., Nash J., D., 2016. Tidally driven processes leading to near-field turbulence in a channel at the crest of the mendocino escarpment. J. Phys. Oceanogr. 1137–1155.

Nagai, T., Tandon, A., Kunze, E., Mahadevan, A., 2015. Spontaneous generation of near-inertial waves by the Kuroshio front. J. Phys. Oceanogr. 45 (9), 2381–2406. http://journals.ametsoc.org/doi/10.1175/JPO-D-14-0086.1.

Nakamura, T., Awaji, T., 2001. A growth mechanism for topographic internal waves generated by an oscillatory flow. J. Phys. Oceanogr. 31 (8), 2511–2524. http://doi.org/10.1175/1520-0485(2001)031<2511:AGMFTI>2.0.CO\n2.

Oke, P.R., Sakov, P., Cahill, M.L., Dunn, J.R., Fiedler, R., Griffin, D.A., Mansbridge, J.V., Ridgway, K.R., Schiller, A., 2013. Towards a dynamically balanced eddy-resolving ocean reanalysis: BRAN3. Ocean Modell. 67, 52–70. http://dx.doi.org/10.1016/j.ocemod.2013.03.008.

Pinkel, R., 2008. Advection, phase distortion, and the frequency spectrum of finescale fields in the sea. J. Phys. Oceanogr. 38 (2), 291–313. http://journals.ametsoc.org/doi/abs/10.1175/2007JPO3559.1.

Rayson, M.D., 2012. The Tidally-driven Ocean Dynamics of the Browse Basin and Kimberley Shelf Region, Ph.D. thesis, Western Australia. University of Western Australia.

Rayson, M.D., Gross, E.S., Fringer, O.B., 2015. Modeling the tidal and sub-tidal hydrodynamics in a shallow, micro-tidal estuary. Ocean Model. 89, 29–44.

Rayson, M.D., Ivey, G.N., Jones, N.L., Meuleners, M.J., Wake, G.W., 2011. Internal tide dynamics in a topographically complex region: Browse Basin, Australian North West Shelf. J. Geophys. Res. Oceans 116.

Rayson, M.D., Jones, N.L., Ivey, G.N., 2012. Temporal variability of the standing internal tide in the Browse Basin, Western Australia. J. Geophys. Res. 117 (C6), C06013. http://doi.wiley.com/10.1029/2011JC007523.

Ridgway, K., Dunn, J., Wilkin, J., 2002. Ocean interpolation by four-dimensional weighted least squares application to the waters around Australasia. J. Atmosp. Oceanic Technol. 19 (9), 1357–1375.

Ringler, T., Petersen, M., Higdon, R.L., Jacobsen, D., Jones, P.W., Maltrud, M., 2013. A multi-resolution approach to global ocean modeling. Ocean Model. 69, 211–232. 10.1016/j.ocemod.2013.04.010.

Sarkar, S., Scotti, A., 2017. From topographic internal gravity waves to turbulence. Annu. Rev. Fluid Mech. 49 (1), 195–220.

Shakespeare, C.J., Hogg, A.M., 2017. Spontaneous surface generation and interior amplification of internal waves in a regional-scale ocean model. J. Phys. Oceanogr. 47 (4), 811–826. http://journals.ametsoc.org/doi/10.1175/JPO-D-16-0188.1.

Shchepetkin, A.F., McWilliams, J.C., 2003. A method for computing horizontal pressure-gradient force in an oceanic model with a nonaligned vertical coordinate. J. Geophys. Res.: Oceans 108 (C3). http://onlinelibrary.wiley.com/doi/10.1029/2001JC001047/full.

Snyder, W.H., Thompson, R.S., Eskridge, R.E., Lawson, R.E., Castro, I.P., Lee, J., Hunt, J.C., Ogawa, Y., 1985. The structure of strongly stratified flow over hills: dividing-streamline concept. J. Fluid Mech. 152, 249–288.

Stephenson, G.R., Green, J.A.M., Inall, M.E., 2016. Systematic bias in baroclinic energy estimates in shelf seas. J. Phys. Oceanogr. 46 (9), 2851–2862. http://journals.ametsoc.org/doi/10.1175/JPO-D-15-0215.1.

Wang, B., Giddings, S.N., Fringer, O.B., Gross, E.S., Fong, D.A., Monismith, S.G., 2011. Modeling and understanding turbulent mixing in a macrotidal salt wedge estuary. J. Geophys. Res. 116 (C2), C02036.

Winters, K.B., Armi, L., 2013. The response of a continuously stratified fluid to an oscillating flow past an obstacle. J. Fluid Mech. 727, 83–118. http://www.journals.cambridge.org/abstract_S0022112013002474.

Wolfram, P.J., Fringer, O.B., 2013. Mitigating horizontal divergence checker-board oscillations on unstructured triangular C-grids for nonlinear hydrostatic and non-hydrostatic flows. Ocean Model. 69, 64–78. http://linkinghub.elsevier.com/retrieve/pii/S1463500313000929.

Zhang, Z., Fringer, O.B., Ramp, S.R., 2011. Three-dimensional, nonhydrostatic numerical simulation of nonlinear internal wave generation and propagation in the South China Sea. J. Geophys. Res.: Oceans 116 (5).